EPJ B
Condensed Matter and Complex Systems
EPJ.org
your physics journal

Eur. Phys. J. B (2016) 89: 169 DOI: 10.1140/epjb/e2016-70226-0

Mechanically driven domain wall movement in magnetoelastic nanomagnets

Théo Mathurin, Stefano Giordano, Yannick Dusch, Nicolas Tiercelin, Philippe Pernod and Vladimir Preobrazhensky

edp sciences
Società Italiana di Fisica
Springer

Eur. Phys. J. B (2016) 89: 169
DOI: 10.1140/epjb/e2016-70226-0

THE EUROPEAN PHYSICAL JOURNAL B

Regular Article

Mechanically driven domain wall movement in magnetoelastic nanomagnets

Théo Mathurin[1], Stefano Giordano[1,a], Yannick Dusch[1], Nicolas Tiercelin[1], Philippe Pernod[1], and Vladimir Preobrazhensky[1,2]

[1] International Associated Laboratory LEMAC/LICS: IEMN, UMR CNRS 8520, ComUE Lille Nord de France, ECLille, Avenue Poincaré, 59652 Villeneuve d'Ascq, France
[2] Wave Research Center, Prokhorov General Physics Institute, Russian Academy of Science, 38 Vavilov str., 119991 Moscow, Russia

Received 12 April 2016 / Received in final form 3 June 2016
Published online 18 July 2016 – © EDP Sciences, Società Italiana di Fisica, Springer-Verlag 2016

Abstract. Magnetic domain walls are fundamental objects arising in ferromagnetic materials, largely investigated both through micromagnetic simulations and experiments. While current- and field-based techniques for inducing domain wall propagation have been widely studied for fundamental understanding and application-oriented purposes, the possibility to manipulate domain walls using mechanical stress in magnetoelastic materials has only recently drawn interest. Here, a complete analytical model describing stress-induced transverse domain wall movement in ferromagnetic nanostripe with variable cross-section is presented. This approach yields a nonlinear integro-differential equation describing the magnetization field. Its numerical implementation, based on the nonlinear relaxation method, demonstrates the possibility to precisely control the position of a domain wall through mechanical action.

1 Introduction

The control of position and motion of ferromagnetic domain walls in nanoscale structures is an emergent subject with relevant applications to magnetic logic [1] and memory devices [2], promising interesting properties such as non-volatility, high integration density, low power consumption and high speed.

Several techniques exist to generate the motion of a ferromagnetic domain wall. Firstly, the domain wall propagation can be induced by external magnetic fields. For instance, the motion of a magnetic domain wall in a submicrometer magnetic wire was detected by use of the giant magnetoresistance effect [3]. Also, room-temperature measurements revealed extremely high propagation velocities of a domain wall in ferromagnetic nanowires [4]. The propagation velocity was proved to show two linear regimes, with the wall mobility at high magnetic fields reduced tenfold from that at low fields [5].

A second technique to induce motion is based on spin-polarized currents. Recently, the velocity of domain walls driven by current in zero magnetic field is measured using real-time resistance measurements. It has been argued that not only spin angular momentum but also linear momentum is transferred to the domain wall from the flow of electrons [6]. Also, the relation between the pinning processes and the threshold current has been investigated in order to propose the engineering of pinning sites to obtain efficient current-induced domain wall manipulation [7]. The best conditions for efficient domain-wall motion by spin-orbit torques have been analyzed. Indeed the overall effect depends critically on the domain-wall configuration, the current injection scheme, and the symmetry of the spin-orbit torque [8]. Moreover, it has been shown that domain wall motion can be initiated by conventional spin-transfer torque and complemented by indirect spin-torque. The latter is created by remote currents and transferred to the domain wall by the exchange-spring mechanism [9].

A third possibility for moving domain walls is based on localized non-uniform mechanical stress. An interesting proposal uses the piezoelectric-piezomagnetic coupling and a series of contacts mimicking the movement of pinning sites. The domain wall moves accordingly, irrespective of the domain wall structure [10]. As a consequence, the domain wall velocity depends on the applied stress gradient [11]. This principle has been realized through practical geometries constituted of piezoelectric phases and spin-valve nanowires. By combining magneto-optical Kerr effect and magnetoresistance measurements, the domain wall propagation fields have been observed and characterized [12].

Other methodologies have been developed through pinning phenomena onto ferroelectric domain walls [13,14] and temperature gradients [15]. Also, the mobility of a current-induced domain wall can be piezoelectrically

[a] e-mail: Stefano.Giordano@iemn.univ-lille1.fr

controlled through a strain-mediated magnetic anisotropy [16]. We remark that a similar research line exists for the dynamics of domain walls in ferroelectric materials [17]. However, the domains behavior in ferroelectrics is at present a very well understood subject. The domains are simple regions separated by Ising-like walls. On the other hand, Bloch or Néel walls in magnets are very complex systems and only recently has their complexity been revealed through transmission electron microscopy, electron holography, atomic force microscopy, magnetic force microscopy and Kerr microscopy [17]. These refined technologies have opened the way to the development of new devices based on magnetic domain walls, ranging from neuromorphic systems [18], spintronic logic [19], racetrack memories [20], memristors [21], to lab-on-chip manipulation of magnetic microbeads [22].

Here, we propose the theoretical and numerical analysis of a Néel domain wall displacement induced by uniform mechanical stress in a nanostripe with variable section. First of all, the use of a purely mechanical action to move the domain wall is very advantageous from the energetic point of view. In fact, current and magnetic field based domain wall motion devices are typically subject to higher energy consumption. Secondly, the procedure used to derive the main equation (see Eq. (30)) is very general and can be applied to other magnetic problems as well. Finally, the technique adopted to solve this equation, based on an iterative method, is very efficient from the numerical point of view. This ad hoc approach allows for a clear physical interpretation of the phenomena involved in our system, without requiring time-consuming micromagnetic simulations [23]. To introduce the proposed physical principle, we consider a uniaxial ferromagnetic nanostripe and we apply an external magnetic field (perpendicular to the stripe itself) to break the symmetry of the two stable magnetization states. So doing, we generate two tilted magnetization states within the material. We assume to have a domain wall between these states. Then, we suppose to further apply a uniform mechanical stress to the two-domain system. As a result, we induce a couple of asymmetrical states and the wall moves so as to expand the domain that is energetically favored and contract the other one.

As recently discussed, the stress can be generated by a piezoelectric substrate [24], by designing a system belonging to the multiferroic heterostructures [25]. While the magnetoelectric coupling in multiferroic structures has been largely studied both experimentally [25] and theoretically in the linear [26,27] and nonlinear [28] regime, the exploitation of the magnetization dynamics in single- and multi- domain systems is a very recent application with important applications in memories, spintronics and new paradigms of information processing. Indeed, it is important to remark that the idea of breaking the symmetry of states in uniaxial magnets has been largely exploited to design memory elements [29–33] and is here generalized to systems with analog behavior. In the first case there is a single magnetic domain and we can switch its magnetization between two asymmetric states. In the second one we have a two-domain system with a domain wall able to move, expanding one domain and narrowing the other. In this work, the switching process is thus replaced by a continuous motion of the wall separating two adjacent domains. Since it has been proved that the stress-mediated control of magnetization allows for excellent energy efficiency in single domain elements, we argue that the mechanical control of the domain walls position is very advantageous for reducing energy consumption [34–38].

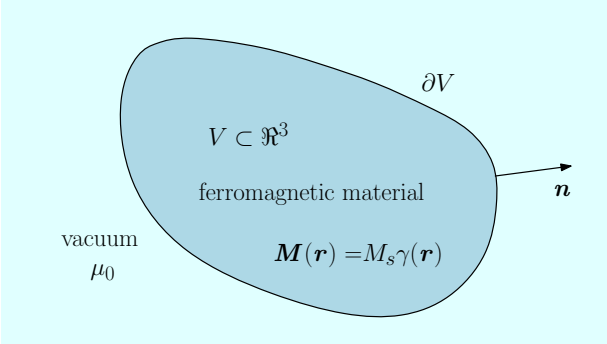

Fig. 1. Geometry of the ferromagnetic material occupying a region V with external surface ∂V and normal unit vector $\boldsymbol{n}$.

The structure of the paper follows. In Section 2, we briefly introduce the micromagnetism formalism for magnetoelastic materials. In particular, we present the classical variational formulation and we describe the methodology adopted to cope with the problem of the demagnetization field. In Section 3, we introduce the physical principles at the origin of the domain wall motion induced by a uniform mechanical stress. We describe the physics and geometry of the system, we perform its energetic analysis and we apply the variational procedure. As a result, we obtain the equation giving the magnetization distribution within the nanostripe. To conclude, in Section 4, we propose a numerical technique to solve this equation, from which we can deduce the position of the domain wall as a function of the applied stress. We finally show a series of results demonstrating the suitability of this concept for innovative devices.

2 Micromagnetism formalism

In this section we present a brief introduction of the micromagnetism formalism [39–41]. In particular, we give a complete assessment of the problem concerning the demagnetization vector field. To begin, we take into consideration a region $V \subset \mathbb{R}^3$ with external surface ∂V and normal unit vector $\boldsymbol{n}$ (see Fig. 1). We suppose that the region V is filled with a ferromagnetic material with magnetoelastic (or magnetostrictive) properties, while the external region $\mathbb{R}^3 \setminus V$ is composed of a linear magnetic material characterized by the vacuum permeability μ_0. The ferromagnetic material is described by a magnetization vector $\boldsymbol{M}$, defined within the region V by its space varying direction $\boldsymbol{\gamma}(\boldsymbol{r})$. It means that $\boldsymbol{M}(\boldsymbol{r}) = M_s\boldsymbol{\gamma}(\boldsymbol{r})$, where M_S represents the magnetization at saturation (a physical

parameter of the ferromagnetic material). We consider the most general form of the energy density stored within the ferromagnetic material. It is composed of the following terms

$$u = u_{an} + u_{ex} + u_{me} + u_{Ze}, \tag{1}$$

where:

– u_{an} represents the anisotropy energy density and takes into consideration specific directions where the magnetization is preferably oriented. This term is due to the crystalline structure of the ferromagnetic material [39]. We consider here an arbitrary form

$$u_{an} = \phi(\boldsymbol{\gamma}). \tag{2}$$

– u_{ex} takes into consideration the exchange interaction among magnetic dipoles of the magnetization distribution. Its general form follows [39]

$$u_{ex} = \frac{1}{2}\alpha_{ij}\frac{\partial\gamma_l}{\partial x_i}\frac{\partial\gamma_l}{\partial x_j}, \tag{3}$$

where $\boldsymbol{\gamma}$ is the magnetization direction and α_{ij} is a symmetric tensor.

– u_{me} is the energy associated to the magnetoelastic effect. Its general form can be written as [39–41]

$$u_{me} = -a_{iklm}T_{ik}\gamma_l\gamma_m = -T_{ik}\epsilon^{\mu}_{ik}. \tag{4}$$

Here, T_{ik} is the Cauchy stress tensor, which is considered known and imposed to the structure[1] and a_{iklm} is a tensor property with the symmetries $a_{iklm} = a_{kilm}$ and $a_{iklm} = a_{ikml}$. The quantity $\epsilon^{\mu}_{ik}(\boldsymbol{\gamma}) = a_{iklm}\gamma_l\gamma_m$ is the so-called eigenstrain characterizing the magnetostrictive effect. It means that the constitutive equation from the elastic point of view is given by $\hat{T} = \hat{L}\left(\hat{\epsilon} - \hat{\epsilon^{\mu}}\right)$, where $\hat{T}$ and $\hat{\epsilon}$ are the actual stress and strain tensors, and $\hat{L}$ is the elastic stiffness tensor (satisfying the same symmetries as $\hat{a}$ plus the additional property $L_{iklm} = L_{lmik}$). This constitutive equation must be interpreted as follows. If the stress is zero (elastically free body), then we find $\hat{\epsilon} = \hat{\epsilon^{\mu}}$, i.e. the real strain corresponds to the eigenstrain, which assumes the character of strain imposed by the magnetization. It means that, when $\boldsymbol{\gamma}$ is fixed in a given region, then $\hat{\epsilon}$ will tend to be equal to $\hat{\epsilon^{\mu}}(\boldsymbol{\gamma})$. In the situation where $\hat{T}$ is not zero (region V constrained or embedded in a given elastic matrix), the actual strain $\hat{\epsilon}$ cannot assume the value $\hat{\epsilon^{\mu}}$, and the system finds a compromise between the effects of magnetization and elastic interactions with the matrix.

– u_{Ze} is the energy corresponding to the local interaction between magnetization and magnetic field. It is called the Zeeman term and its general expression is [42]

$$u_{Ze} = -\mu_0 M_S\, \boldsymbol{H}_L \cdot \boldsymbol{\gamma}. \tag{5}$$

It is important to underline that $\boldsymbol{H}_L$ is the *local* magnetic field that one can measure at any given point $\boldsymbol{r}$. Typically, it is composed of two contributions: an externally applied field $\boldsymbol{H}_0$ and a magnetic field $\boldsymbol{H}_d$ generated by the magnetization distribution $\boldsymbol{M}(\boldsymbol{r})$ itself. The latter is referred to as the demagnetization field. Therefore, we have $\boldsymbol{H}_L = \boldsymbol{H}_0 + \boldsymbol{H}_d$, where $\boldsymbol{H}_d$ directly depends on $\boldsymbol{\gamma}(\boldsymbol{r})$.

We can finally introduce the total energy stored within the region V

$$U = \int_V u\, dv = \int_V (u_{an} + u_{ex} + u_{me} + u_{Ze})\, dv. \tag{6}$$

In this expression, U depends on the function $\boldsymbol{\gamma} = \boldsymbol{\gamma}(\boldsymbol{r})$, while $\hat{T}$ and $\boldsymbol{H}_L$ are imposed quantities. The behavior of the region V can be summarized through the following principle: the magnetization distribution within V must be found by minimizing U with respect to $\boldsymbol{\gamma}(\boldsymbol{r})$, with $\hat{T}(\boldsymbol{r})$ and $\boldsymbol{H}_L(\boldsymbol{r})$ fixed. From the mathematical point of view, this is a problem of the calculus of variations. However, this approach is hardly applicable to real situations since, typically, we are able to fix the external field $\boldsymbol{H}_0$, but we can not control the total field $\boldsymbol{H}_L$. Indeed, the demagnetization field $\boldsymbol{H}_d$ depends on $\boldsymbol{\gamma} = \boldsymbol{\gamma}(\boldsymbol{r})$ being the sum of all contributions generated by the elementary dipoles of the overall distribution [42]

$$\boldsymbol{H}_d(\boldsymbol{r}) = M_S \int_V \hat{N}(\boldsymbol{r}, \boldsymbol{r}_0)\, \boldsymbol{\gamma}(\boldsymbol{r}, \boldsymbol{r}_0)\, d\boldsymbol{r}_0, \tag{7}$$

with

$$\hat{N}(\boldsymbol{r}, \boldsymbol{r}_0) = \frac{1}{4\pi}\left[\frac{3(\boldsymbol{r} - \boldsymbol{r}_0) \otimes (\boldsymbol{r} - \boldsymbol{r}_0)}{\|\boldsymbol{r} - \boldsymbol{r}_0\|^5} - \frac{\hat{I}}{\|\boldsymbol{r} - \boldsymbol{r}_0\|^3}\right]. \tag{8}$$

In equation (8), $\boldsymbol{a} \otimes \boldsymbol{b}$ represents the tensor product between two vectors $\boldsymbol{a}$ and $\boldsymbol{b}$, i.e. $(\boldsymbol{a} \otimes \boldsymbol{b})_{ij} = a_i b_j$, and $\hat{I}$ is the identity operator. One can prove that $\hat{N}$ exhibits the symmetries

$$\hat{N}(\boldsymbol{r}, \boldsymbol{r}_0) = \hat{N}^T(\boldsymbol{r}, \boldsymbol{r}_0), \tag{9a}$$

$$\hat{N}(\boldsymbol{r}, \boldsymbol{r}_0) = \hat{N}(\boldsymbol{r}_0, \boldsymbol{r}). \tag{9b}$$

The above principle suggests to minimize U with $\hat{T}$ and $\boldsymbol{H}_L$ fixed. We have to prove an equivalent result based on a different functional $\tilde{U}$ minimized with $\hat{T}$ and $\boldsymbol{H}_0$ fixed. In other words, we search for a new functional $\tilde{U}$ satisfying the following equivalence

$$\min_{\boldsymbol{\gamma}\,:\,\|\boldsymbol{\gamma}\|=1} U\Big|_{\boldsymbol{H}_L \text{ fixed}} \Leftrightarrow \min_{\boldsymbol{\gamma}\,:\,\|\boldsymbol{\gamma}\|=1} \tilde{U}\Big|_{\boldsymbol{H}_0 \text{ fixed}}. \tag{10}$$

We prove in Appendix A that the exact mathematical form of $\tilde{U}$ is the following

$$\tilde{U} = \int_V \left[\phi(\boldsymbol{\gamma}) + \frac{1}{2}\alpha_{ij}\frac{\partial\gamma_l}{\partial x_i}\frac{\partial\gamma_l}{\partial x_j} - T_{ik}\epsilon^{\mu}_{ik} + \mu_0 M_S H_{0i}\gamma_i\right] dv - \int_V \int_V \frac{1}{2}\mu_0 M_S^2 \boldsymbol{\gamma}(\boldsymbol{r}) \cdot \hat{N}(\boldsymbol{r}, \boldsymbol{r}_0)\boldsymbol{\gamma}(\boldsymbol{r}_0) d\boldsymbol{r}_0 d\boldsymbol{r}, \tag{11}$$

[1] The problem of determining the actual stress distribution in V, when the body is embedded in a different elastic environment is treated elsewhere and not considered in the present development (see, e.g., Ref. [34]).

where the last term represents the demagnetization energy. The minimization of $\tilde{U}$ with respect to the direction $\boldsymbol{\gamma}$, with $\hat{T}$ and $\boldsymbol{H}_0$ imposed, leads to the actual magnetization of the ferromagnetic body. Incidentally, it is interesting to point out that this mathematical problem completely describes the emergence of the domains structure typical of the ferromagnetic materials. The result of this minimization, proved in Appendix A, follows

$$\boldsymbol{\gamma} \times \boldsymbol{H}_{eff} = 0, \tag{12}$$

where

$$\boldsymbol{H}_{eff} = \boldsymbol{H}_0 + \boldsymbol{H}_d - \frac{1}{\mu_0 M_S}\frac{\partial \phi}{\partial \boldsymbol{\gamma}} + \frac{\alpha_{ij}}{\mu_0 M_S}\frac{\partial^2 \boldsymbol{\gamma}}{\partial x_i \partial x_j} + \frac{2}{\mu_0 M_S}\hat{a} : \hat{T}\boldsymbol{\gamma}. \tag{13}$$

These results are in perfect agreement with classical developments [39–41,43,44]. On the external surface of the region V we must impose the boundary conditions (see again Appendix A for details)

$$\alpha_{ij}\epsilon_{lst}\gamma_t \frac{\partial \gamma_l}{\partial x_j} n_i = 0 \quad \forall\, s \quad \text{on} \quad \partial V. \tag{14}$$

In particular, with isotropic exchange ($\alpha_{ij} \propto \delta_{ij}$), the boundary conditions simplify to

$$\frac{\partial \boldsymbol{\gamma}}{\partial n} = 0 \quad \text{on} \quad \partial V. \tag{15}$$

To conclude, the behavior of the ferromagnetic region V can be summarized by observing that equation (12) must be satisfied in V with boundary conditions stated in equation (14) for the general case, or in equation (15) for isotropic exchange. Of course, the boundary conditions must be substituted with $\boldsymbol{\gamma}(\boldsymbol{r}) = f(\boldsymbol{r})$ for $\boldsymbol{r} \in \partial V$ when the magnetization is imposed on ∂V.

3 Mechanical control of domain wall position

In this section, we describe the application of the previous formalism (with some modifications) to demonstrate the possibility to control the position of a domain wall through a uniform mechanical stress in uniaxial ferromagnets.

3.1 Description of the system

The general geometry of the ferromagnetic system is shown in Figure 2. It is constituted by a nanostripe of thickness h, length L and variable width $\ell(x)$. Two hypotheses will be assumed for analyzing the system: (i) the magnetization $\boldsymbol{M}$ lies in the (x, y) plane, and (ii) the magnetization depends only on x. Hence, we have

$$\boldsymbol{M}(\boldsymbol{r}) = M_S\,(\cos\theta(x), \sin\theta(x), 0)\,, \tag{16}$$

where $\theta(x)$ is the angle between $\boldsymbol{M}$ and the x-axis. These hypotheses are reasonable as long as the thickness and width of the nanomagnet are small compared to its length (nanostripe geometry). Moreover, we can anticipate that the shape function $\ell(x)$ used to stabilize the wall position is very slightly variable with x, consistently with our assumptions. We also underline that assumptions (i) and (ii) have been used in the past to study the motion of a domain wall induced by an external magnetic field. In this case the model yielded results in good agreement with experiments [45].

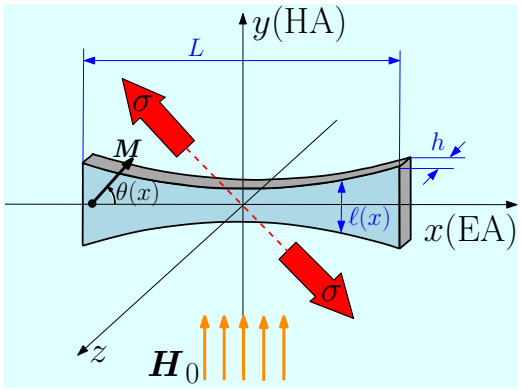

Fig. 2. Ferromagnetic nanostripe characterized by a variable cross-section $h\ell(x)$. The ferromagnetic easy-axis (EA) is aligned with the x-axis, while the hard-axis (HA) corresponds to the y-axis. The magnetization $\boldsymbol{M}$ is described by the angle $\theta(x)$ (measured anticlockwise) and the magnetic field $\boldsymbol{H}_0$ and mechanical action σ are applied to the system.

As described in Figure 2, we consider a material with uniaxial behavior, having the easy-axis (EA) aligned to the x-axis and the hard-axis (HA) aligned to the y-axis. It means that the angles $\theta = 0$ and $\theta = \pi$ correspond to two stable positions $\boldsymbol{M}_1$ and $\boldsymbol{M}_2$ of the magnetization under the sole influence of the anisotropy (see Fig. 3). In these conditions ($\boldsymbol{H}_0 = 0$ and $\sigma = 0$), we consider a Néel domain wall positioned at $x = 0$ (see Fig. 4). It is created by the imposed boundary conditions (see Sect. 3.3 for details) and it is stable because of the symmetrical shape function having minimal cross section for $x = 0$. The external magnetic field is a crucial element for the working principle of the proposed system. Indeed, when we apply $\boldsymbol{H}_0$ along the y-axis, the stable orientations of the magnetization are tilted in the direction of the field, obtaining $\boldsymbol{M}_1'$ and $\boldsymbol{M}_2'$, as shown in Figure 3. We remark that $\boldsymbol{M}_1'$ and $\boldsymbol{M}_2'$ are still symmetric. Hence, the domain wall remains in the position $x = 0$ since the energy density is the same in the two domains. This position is therefore still stable. Further, if we also apply the mechanical uniform stress σ, along the bisector of the second quadrant as indicated in Figure 2, the new magnetization vectors $\boldsymbol{M}_1''$ and $\boldsymbol{M}_2''$ lose their symmetry, as shown in Figure 3 (for both $\sigma > 0$ and $\sigma < 0$). In this situation the energy density is not the same within the two domains. Therefore, the domain wall moves in order to reduce the size of the domain with higher energy density. The domain wall motion stops only when the total energy reaches its minimum (see Sect. 2), corresponding to the new equilibrium for the system.

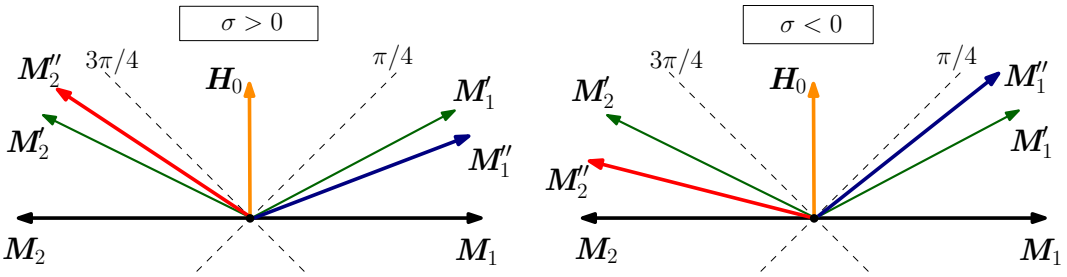

Fig. 3. Stable magnetization states within the nanostripe. The uniaxial anisotropy without $\boldsymbol{H}_0$ and σ induces two opposite states $\boldsymbol{M}_1$ and $\boldsymbol{M}_2$. When $\boldsymbol{H}_0$ is applied, we have $\boldsymbol{M}'_1$ and $\boldsymbol{M}'_2$, still symmetric. Further, the mechanical stress leads to the tilted states $\boldsymbol{M}''_1$ and $\boldsymbol{M}''_2$, which are asymmetric for both $\sigma > 0$ and $\sigma < 0$.

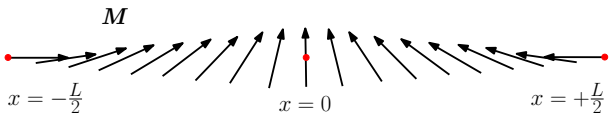

Fig. 4. Typical magnetic distribution in a Néel wall as considered within the nanostripe.

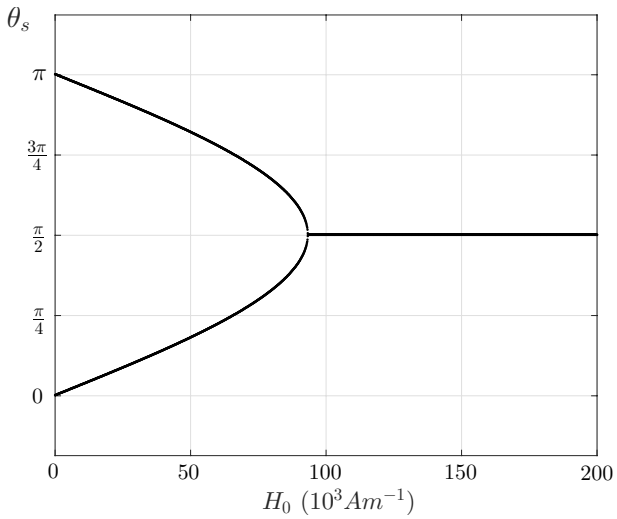

Fig. 5. Effect of the magnetic field on the stable states of the system (with $\sigma = 0$). The two angles get closer as H_0 increases until only one stable position remains ($\theta = \frac{\pi}{2}$) for $H_0 \geq H_a$.

We underline that the influence of the applied magnetic field is essential for the mechanical stress to induce movement since it tilts the states with respect to the x direction. Indeed, without a significant magnetic field, the role of the Zeeman energy can be disregarded and the application of the mechanical stress leaves the two states indistinguishable (from the energetic point of view). At the same time, the magnetic field intensity should not be larger than a given threshold, otherwise the anisotropy energy becomes negligible, leaving a single stable state corresponding to $\theta = \frac{\pi}{2}$. In Figure 5 we show the angles θ_s of the stable states as a function of the applied field H_0, with $\sigma = 0$. One can clearly see the typical bifurcation for a critical value of H_0, referred to as H_a (see below for details). We have $\theta_s = \theta_1$ or θ_2 (corresponding to $\boldsymbol{M}'_1$ and $\boldsymbol{M}'_2$) if $H_0 < H_a$ and $\theta_s = \pi/2$ if $H_0 > H_a$. These

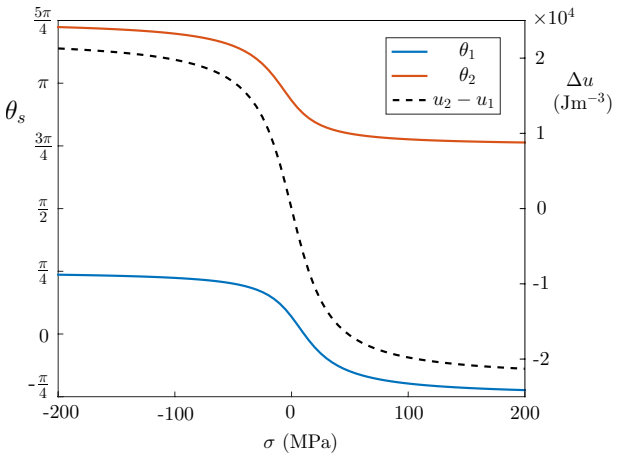

Fig. 6. Angles θ_1 and θ_2 of stable magnetization orientations as a function of the mechanical stress σ, and energy density gap $\Delta u = u_2 - u_1$ between the corresponding states.

considerations yield quantitative constraints to the design of the proposed system. From the point of view of the implementation, the field H_0 can be realized through micropatterned permanent nanomagnets [46], which do not participate to the energy consumption.

As discussed above, the mechanism driving domain wall motion when applying a mechanical stress lies in the energy asymmetry. Indeed, the tilt generated on the magnetization vectors of the domains is such that they are distinguishable from the energetic point of view. In Figure 6 one can find the values of stables positions θ_1 and θ_2 (corresponding to $\boldsymbol{M}''_1$ and $\boldsymbol{M}''_2$) as functions of the applied stress, as well as the energy density gap induced between the two domains (for a given $H_0 \neq 0$). This gap has been calculated by adding Zeeman, anisotropy and magnetoelastic energies. In this preliminary discussion we neglected the demagnetization and exchange energies, deeply discussed below. Anyway, we observe that the energy density gap increases in absolute value with increasing mechanical stress, showing saturation for $\sigma \to \pm\infty$. To better understand the working principle of the system we also show in Figure 7 the energy density landscape, i.e. the energy density of a domain in terms of the angle θ characterizing the magnetization and the applied magnetic field H_0. We can observe the intrinsic bistability of the system under the threshold H_a of magnetic field and the effect of the

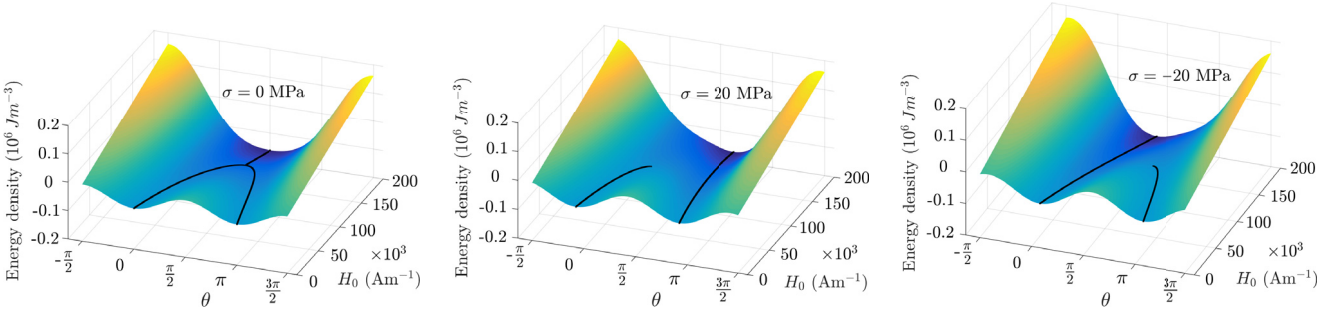

Fig. 7. Energy landscape as a function of the magnetization angle θ and applied magnetic field H_0. The application of a stress modifies the stable magnetization states and their energy densities, favoring a given state over the other one. In the first panel we considered $\sigma = 0$, in the second one $\sigma > 0$ and in the third one $\sigma < 0$.

mechanical stress, which generates an energy gap between the stable states (only when $H_0 \neq 0$). In general, depending on the geometry adopted, the motion induced by σ can either continue indefinitely or stop at a given equilibrium position. We proved that for a nanostripe with uniform section it is impossible to stabilize the position for all stress values (see below). On the other hand, the geometry with larger section close to the extremities may guarantee the existence of an equilibrium position for the domain wall, preventing it from reaching the extremities and thus being ejected. Indeed, the domain wall has an intrinsic surface energy (proportional to the wall area), which participates to the total system energy. This point substantiates the shape of the ferromagnetic nanostripe shown in Figure 2. It is worth noting that in real experimental setups, several techniques have been studied and are routinely used to create pinning sites to stabilize magnetic domain walls. They include inhomogeneities [47] or structural defects [48–51], and geometrical notches [52,53]. Here, we follow an alternative way to prevent domain wall ejection based on the variable cross-section.

3.2 Energetic analysis

As previously discussed, the first step of the system analysis consists in writing the overall energy of the system, composed of anisotropy, Zeeman, magnetoelastic, exchange and demagnetization contributions.

To begin with, let us consider the anisotropic uniaxial behavior described by the energy density

$$u_{an} = -K_u \gamma_x^2 = -K_u \cos^2\theta. \tag{17}$$

Moreover, because of the uniaxial symmetry of the ferromagnet, the exchange energy described in equation (3) simplifies by considering two different constants $\alpha_{11} = 2A$ and $\alpha_{22} = \alpha_{33} = 2B$ ($\alpha_{ij} = 0\ \forall\, i \neq j$). Explicitly, we have

$$u_{ex} = A\left(\frac{\partial \boldsymbol{\gamma}}{\partial x}\right)^2 + B\left[\left(\frac{\partial \boldsymbol{\gamma}}{\partial y}\right)^2 + \left(\frac{\partial \boldsymbol{\gamma}}{\partial z}\right)^2\right]. \tag{18}$$

With the assumption in equation (16), we easily get

$$u_{ex} = A\left(\frac{\partial \theta}{\partial x}\right)^2. \tag{19}$$

As stated in previous description of the system, the applied magnetic field is considered aligned with the y-axis, leading to the following contribution

$$u_{Ze} = -\mu_0 M_S \boldsymbol{H}_0 \cdot \boldsymbol{\gamma} = -\mu_0 M_S H_0 \sin\theta, \tag{20}$$

where we considered only the externally applied field $\boldsymbol{H}_0$. The demagnetization field will be treated separately. Let us now discuss the mechanical stress and the corresponding magnetoelastic energy. First of all, the mathematical form of the magnetostriction $\hat{\epsilon}^\mu(\boldsymbol{\gamma})$ should be defined. It corresponds to the strain tensor associated with the magnetization direction $\boldsymbol{\gamma}$ for a body free of stress. A displacement field describing a uniform deformation along $\boldsymbol{\gamma}$ can be written as $\boldsymbol{u}(\boldsymbol{x}) = \epsilon_l \boldsymbol{\gamma}(\boldsymbol{x}\cdot\boldsymbol{\gamma})$, where ϵ_l is the so-called longitudinal deformation. On the other hand, a displacement field corresponding to a uniform transversal deformation ϵ_t is given by $\boldsymbol{u}(\boldsymbol{x}) = \epsilon_t\,[\boldsymbol{x} - \boldsymbol{\gamma}(\boldsymbol{x}\cdot\boldsymbol{\gamma})]$. The sum of the two contributions leads to an eigenstrain $\epsilon^\mu_{ij} = \epsilon_l \gamma_i\gamma_j + \epsilon_t(\delta_{ij} - \gamma_i\gamma_j)$. It has been well established that the magnetostriction is an isovolumic process and thus we impose $\mathrm{Tr}\hat{\epsilon}^\mu = 0$, i.e. $\epsilon^\mu_{ii} = \epsilon_l + 2\epsilon_t = 0$, from which it follows that $\epsilon_t = -\frac{\epsilon_l}{2}$. By defining $\lambda_S = \epsilon_l$, typically referred to as the magnetostriction coefficient, we have

$$\epsilon^\mu_{ij} = \frac{\lambda_S}{2}(3\gamma_i\gamma_j - \delta_{ij}), \tag{21}$$

and the general form of the magnetostrictive energy is

$$u_{me} = -\hat{T} : \epsilon^\mu = -\tfrac{\lambda_S}{2}\left(3\gamma_i\gamma_j T_{ij} - T_{ii}\right). \tag{22}$$

As an example, if $T_{22} = \sigma$ and the other components are zero,

$$u_{me} = -\frac{3}{2}\lambda_S \sigma \gamma_2^2 + const. \tag{23}$$

In our system, a unidirectional stress is applied along the direction identified by $\theta = -\frac{\pi}{4}$ (bisector of the second quadrant). In order to obtain the corresponding energy density, it is convenient to work in the frame (x', y') tilted with respect to (x, y) by an angle of $\frac{\pi}{4}$. Hence, we have $\boldsymbol{\gamma} = \cos(\theta - \frac{\pi}{4})\,\boldsymbol{e}_{x'} + \sin(\theta - \frac{\pi}{4})\,\boldsymbol{e}_{y'}$. Here, $\boldsymbol{e}_{x'}$ and $\boldsymbol{e}_{y'}$ are the unit vectors in directions x' and y', respectively. Now, in the (x', y') frame we have a unidirectional stress along the y'-axis and, therefore, the energy density is given

by equation (23), with $\gamma_2^2 = \sin^2(\theta - \frac{\pi}{4}) = -\sin\theta\cos\theta + const.$ Finally, the energy density is

$$u_{me} = \frac{3}{2}\lambda_S \sigma \sin\theta\cos\theta, \tag{24}$$

where we neglected the irrelevant additive constant. To sum up, the total energy density of the system is

$$\begin{aligned} u = &- K_u \cos^2\theta + A\left(\frac{d\theta}{dx}\right)^2 - \mu_0 M_S H_0 \sin\theta \\ &+ \frac{3}{2}\lambda_S\sigma\sin\theta\cos\theta - \frac{1}{2}\mu_0 M_S \boldsymbol{H}_d\cdot\boldsymbol{\gamma}, \end{aligned} \tag{25}$$

where the last term represents the demagnetization energy density, as shown in equation (11). The total energy U can be finally calculated by integrating equation (25) over the ferromagnetic region

$$\begin{aligned} U = &\int_{-\frac{L}{2}}^{\frac{L}{2}} h\ell(x)\left[-K_u\cos^2\theta + A\left(\frac{d\theta}{dx}\right)^2\right. \\ &\left. - \mu_0 M_S H_0\sin\theta + \frac{3}{2}\lambda_S\sigma\sin\theta\cos\theta\right]dx \\ &- \int_V\int_V \frac{1}{2}\mu_0 M_S^2 \boldsymbol{\gamma}(\boldsymbol{r})\cdot\hat{N}(\boldsymbol{r},\boldsymbol{r}_0)\boldsymbol{\gamma}(\boldsymbol{r}_0)\,d\boldsymbol{r}_0 d\boldsymbol{r}, \end{aligned} \tag{26}$$

where the cross section $h\ell(x)$ has been introduced for integrating the first four terms (where the energy density depends only on x).

3.3 Variational procedure

Let us consider the total energy U as a functional of $\theta(x)$. The Gâteaux derivative [54] of U can be written as follows

$$\begin{aligned} &\frac{d}{d\alpha}\,U\left(\theta(x)+\alpha k(x)\right)\Big|_{\alpha=0} \\ &= \int_{-\frac{L}{2}}^{\frac{L}{2}} h\ell(x)\left[K_u\sin(2\theta)k(x) - \mu_0 M_S H_0\cos\theta k(x)\right. \\ &\quad \left. + \frac{3}{2}\lambda_S\sigma\cos(2\theta)k(x) + 2A\frac{d\theta}{dx}\frac{dk}{dx}\right]dx \\ &\quad - \frac{1}{2}\mu_0 M_S^2\left(\int_V\int_V \frac{\partial\boldsymbol{\gamma}}{\partial\theta}(x)\cdot\hat{N}(\boldsymbol{r},\boldsymbol{r}_0)\boldsymbol{\gamma}(x_0)k(x)d\boldsymbol{r}_0 d\boldsymbol{r}\right. \\ &\quad \left. + \int_V\int_V \boldsymbol{\gamma}(x)\cdot\hat{N}(\boldsymbol{r},\boldsymbol{r}_0)\frac{\partial\boldsymbol{\gamma}}{\partial\theta}(x_0)d\boldsymbol{r}_0 d\boldsymbol{r}\right), \end{aligned} \tag{27}$$

where α is a real parameter and $k(x)$ is the perturbation function. The exchange term can be elaborated through an integration by parts. Moreover, the two demagnetization terms in the fourth and fifth lines of equation (27) are identical, as can be proved by exploiting symmetries of tensor $\hat{N}$ stated in equations (9a) and (9b). Hence, the demagnetization term, referred to as $\mathcal{D}$, can be rewritten as

$$\begin{aligned} \mathcal{D} &= -\mu_0 M_S^2 \int_V\int_V \frac{\partial\boldsymbol{\gamma}}{\partial\theta}(x)\cdot\hat{N}(\boldsymbol{r},\boldsymbol{r}_0)\boldsymbol{\gamma}(x_0)k(x)d\boldsymbol{r}_0 d\boldsymbol{r} \\ &= -\mu_0 M_S \int_V \frac{\partial\boldsymbol{\gamma}}{\partial\theta}(x)\cdot\boldsymbol{H}_d(\boldsymbol{r})k(x)d\boldsymbol{r} \\ &= -\mu_0 M_S \int_{-\frac{L}{2}}^{+\frac{L}{2}} h\ell(x)\frac{\partial\boldsymbol{\gamma}}{\partial\theta}(x)\cdot\langle\boldsymbol{H}_d\rangle_{y,z}\,k(x)\,dx, \end{aligned} \tag{28}$$

where

$$\langle\boldsymbol{H}_d\rangle_{y,z} = \frac{1}{h\ell(x)}\int_{-\frac{\ell(x)}{2}}^{+\frac{\ell(x)}{2}}\int_{-\frac{h}{2}}^{+\frac{h}{2}} \boldsymbol{H}_d(\boldsymbol{r})dzdy$$

is the average value of the field $\boldsymbol{H}_d$ over the cross section at x constant. By substituting equation (28) in equation (27) we eventually get

$$\begin{aligned} &\frac{d}{d\alpha}\,U\left(\theta(x)+\alpha k(x)\right)\Big|_{\alpha=0} \\ &= \int_{-\frac{L}{2}}^{+\frac{L}{2}} h\ell\left[2K_u\sin(2\theta) - \mu_0 M_S H_0\cos\theta + \frac{3}{2}\lambda_S\sigma\cos 2\theta\right]kdx \\ &\quad - \int_{-\frac{L}{2}}^{+\frac{L}{2}} 2hA\left(\frac{d\ell}{dx}\frac{d\theta}{dx} + \ell\frac{d^2\theta}{d^2x}\right)k\,dx + \left[2hA\ell\frac{d\theta}{dx}k\right]_{-\frac{L}{2}}^{+\frac{L}{2}} \\ &\quad - \mu_0 M_S \int_{-\frac{L}{2}}^{+\frac{L}{2}} h\ell\frac{\partial\boldsymbol{\gamma}}{\partial\theta}\cdot\langle\boldsymbol{H}_d\rangle_{y,z}\,k\,dx. \end{aligned} \tag{29}$$

Now, since we wish to study the motion of a domain wall in the interval $\left[-\frac{L}{2},+\frac{L}{2}\right]$, the function θ assumes fixed finite values at $\theta\left(-\frac{L}{2}\right)$ and $\theta\left(+\frac{L}{2}\right)$, which correspond to the stable magnetization states mentioned above. As a consequence, the perturbation function k must vanish at the interval end-points $x = \pm\frac{L}{2}$. Hence, equation (29) is zero for any real function k when

$$\begin{aligned} &\frac{d^2\theta}{d^2x} + \frac{1}{\ell(x)}\frac{d\ell(x)}{dx}\frac{d\theta}{dx} - \frac{\mu_0 M_s}{2A}\left[\frac{K_u}{\mu_0 M_s}\sin(2\theta)\right. \\ &\qquad - H_0\cos\theta + \frac{3}{2}\frac{\lambda_S\sigma}{\mu_0 M_s}\cos(2\theta) \\ &\qquad \left. + \sin\theta\langle H_{dx}\rangle_{y,z} - \cos\theta\langle H_{dy}\rangle_{y,z}\right] = 0. \end{aligned} \tag{30}$$

This is the main equation governing the behavior of the magnetization orientation within the structure considered.

From the mathematical point of view it is a second order integro-differential equation with fixed boundary conditions ($\langle \boldsymbol{H}_d \rangle_{y,z}$ depends on θ through an integral operation). The original character of this equation can be underlined by observing that it describes a one-dimensional model but, at the same time, its second term in equation (30) takes into account the actual shape of the ferromagnetic region (through the variable width ℓ). This point also represents the crucial modification introduced with respect to the classical development summarized in Section 2. Therefore, this approach, specifically elaborated for the study of a nanostripe with a two-domain structure, allows for the wall motion analysis with a strong reduction of the necessary computational effort with respect to, e.g., a standard finite element micromagnetic approach. The latter, while allowing to tackle a wide variety of magnetic problems, is less computationally efficient for such a simple system.

The orientations of the magnetization at both boundaries of the nanostripe can be imposed by considering the states $\boldsymbol{M}_1''$ and $\boldsymbol{M}_2''$, introduced in Section 3.1. The corresponding angles can be found by using equation (30) where we neglect exchange and demagnetization terms. The resulting equation can be written as

$$K_u \sin(2\theta) - \mu_0 M_S H_0 \cos\theta + \frac{3}{2}\lambda_S \sigma \cos(2\theta) = 0. \quad (31)$$

This equation provides two angles corresponding to the stable states generated by the combination of anisotropy, applied magnetic field and mechanical stress. By defining $t = \tan(\theta/2)$, we get a fourth-degree algebraic equation, which can be numerically solved with standard techniques. We can also take into consideration the simpler boundary conditions $\theta(-L/2) = 0$ and $\theta(+L/2) = \pi$, fixed for any value of the mechanical stress σ. The comparison of results obtained with the two different types of boundary conditions is useful to understand their effect on the overall behavior of the system.

4 Numerical implementation and results

The main equation derived above must be numerically solved to get the desired solution representing the angle profile $\theta(x)$. We describe here in detail the numerical approach implemented alongside its results. We anticipate that all numerical calculations have been carried out with a given set of physical properties corresponding to the magnetoelastic material Terfenol. Accordingly, we used a magnetization saturation $M_s = 64 \times 10^4$ A/m [34], an exchange interaction coefficient $A = 9 \times 10^{-12}$ A/m [55]. We also adopt an anisotropy constant $K_u = 37.5 \times 10^3$ J/m^3 corresponding to an anisotropy field $H_a = 92 \times 10^3$ A/m (defined through the expression $K_u = \frac{1}{2}\mu_0 M_s H_a$), which can be easily obtained in real ferromagnetic layers [30]. We remark that H_a represents the bifurcation threshold shown in Figure 5. The strong magnetostriction in Terfenol is characterized by a coefficient $\lambda_S = 1 \times 10^{-3}$ [56]. Moreover, an applied field $H_0 = 20 \times 10^3$A/m is used throughout all simulations. These values have been also used in Figures 5–7.

4.1 Nonlinear relaxation

The aim of this section is to describe the numerical method proposed to solve equation (30). This is a nonlinear second order integro-differential equation with fixed boundary conditions. Therefore, we can use a nonlinear relaxation method, or iterative technique [57]. This approach is based on a spatial discretization of the interval $[-L/2, +L/2]$ with N points, where $x_1 = -L/2$ and $x_N = L/2$. Thus we define $\Delta x = \frac{L}{N-1}$. All physical variables used in our procedure will be calculated according to this discretization.

The only non-trivial term to compute is the demagnetization contribution. As a matter of fact, the demagnetization field at each point depends on the magnetization of the whole ferromagnetic body, which, in addition, changes at each iteration. Therefore, a straightforward implementation is likely to be computationally intensive. Here, we consider the sequence of $N-1$ regions $[x_i, x_{i+1}] \times [-\frac{l(x_i)}{2}, +\frac{l(x_i)}{2}] \times [-\frac{h}{2}, +\frac{h}{2}]$ for $i \in \{1, \ldots, N-1\}$. The contribution of each region to the demagnetization field can be calculated through closed form expressions, as demonstrated in Appendix B. Then, the total demagnetization field, measured at any given point, is simply the sum of all contributions generated by all parallepepipedal regions. Of course, we introduce a small systematic error due to the fact that the system with variable cross-section can be only approximately represented by the juxtaposition of all the parallelepipeds. However, the approximation is very good for a low derivative $\ell'(x)$. It is important to notice that this scheme ensures a relatively efficient computation since in equations (B.19) and (B.20) of Appendix B the geometry (derivatives of $\mathcal{F}$ function) and physics (magnetization) can be decoupled so that geometry dependant factors are calculated once and for all before the run (i.e., off-line).

We define θ_i^m as the unknown angle for $x = x_i = -L/2 + (i-1)\Delta x$ and calculated at the mth iteration. Since $\theta_1 = \theta(x_1) = \theta(-L/2)$ and $\theta_N = \theta(x_N) = \theta(+L/2)$ are fixed, we can start the procedure with a given guess function θ_i^0, $i = 1, \ldots, N$ (such that $\theta_1^0 = \theta(-L/2)$ and $\theta_N^0 = \theta(+L/2)$), and then proceed by iterations [57]. Indeed, we observe that equation (30) can be written in a discretized way as follows

$$\begin{aligned} 0 = {} & \frac{1}{\Delta x^2}\left(\theta_{i+1}^m - 2\theta_i^{m+1} + \theta_{i-1}^m\right) \\ & + \frac{1}{2\Delta x}\left(\theta_{i+1}^m - \theta_{i-1}^m\right)\frac{\ell_i'}{\ell_i} \\ & - \frac{\mu_0 M_S}{2A}\left[\frac{K_u}{\mu_0 M_S}\sin 2\theta_i^{m+1}\right. \\ & - H_0 \cos\theta_i^{m+1} + \frac{3}{2}\frac{\lambda_S \sigma}{\mu_0 M_S}\cos 2\theta_i^{m+1} \\ & \left. + \sin\theta_i^{m+1}\langle H_{dx}\rangle_{y,z} - \cos\theta_i^{m+1}\langle H_{dy}\rangle_{y,z}\right], \quad (32) \end{aligned}$$

where the unknown quantity at each iteration is $\theta_i^{m+1}\ \forall i$, and the index m relates to quantities coming from the previous iteration. As an example, the guess function can be considered as the linear function imposed by θ_1 and θ_N. The previous equation (32) is a transcendental nonlinear equation, which must be solved numerically. To solve this problem, we can reasonably use the bisection method, which allows for both fast convergence and arbitrarily high precision. Moreover, the terms $\langle H_{dx}\rangle_{y,z}$ and $\langle H_{dy}\rangle_{y,z}$ can be computed by means of the magnetization distribution at the m-th step. Two parameters are introduced to control the convergence criteria of the bisection method and the iterative procedure itself, respectively.

In order to check the performances of the proposed numerical technique and, in particular, its convergence toward the right solution, we considered a simple case that can be handled analytically. It corresponds to a nanostripe with constant width, where we only take exchange and anisotropy contributions into account. In this case the solution is given by the following closed form expressions

$$\sqrt{\frac{K_u}{A}}\left(x+\frac{L}{2}\right)=\frac{1}{\xi}F\left(\arcsin\frac{\xi\sin\theta}{\sqrt{\xi^2-\cos^2\theta}},\frac{1}{\xi}\right), \quad (33)$$

$$\frac{1}{\xi}K\left(\frac{1}{\xi}\right)=\frac{L}{2}\sqrt{\frac{K_u}{A}}, \quad (34)$$

which are proved in Appendix C (where we also define the elliptic functions F and K). The second equation must be solved with respect to the parameter ξ and then the first one gives the relation between x and θ characterizing the specific domain wall under investigation (for details see Appendix C). We underline that this result is consistent with classical expressions obtained considering $L \to +\infty$ [39]. This solution is now used to check the numerical technique by direct comparison. We consider a uniform nanostripe with $h = 20$ nm, $\ell = 40$ nm and $L = 400$ nm. As one can see in Figure 8, the numerical procedure correctly converges toward the expected solution. We used the linear guess to initialize the iterative procedure. In the inset of Figure 8 we have also shown the relative error δ (the difference in norm between steps m and $m+1$), which tends to zero, proving the Cauchy convergence of the sequence [54]. The stopping criterion of the iterative process is based on a threshold value of δ, referred to as $\delta_{\min}$ (here we used $\delta_{\min} = 10^{-20}$).

The convergence of the procedure can be more closely monitored by quantifying the absolute error ϵ defined as the difference between the numerical and the theoretical solution. We considered different level of discretization, analyzed with the same stopping criterion based on $\delta_{\min} = 10^{-20}$. In Figure 9 we show ϵ as a function of the number of points N used in the discretization. The relationship between the two is clearly represented by a power law, the exponent being about -4. This value of the exponent remains constant by varying the parameters A and K_u of the problem, thereby proving a universal convergence. As usual, one has to find a compromise between accuracy and calculation time. Indeed, by increasing the number of points we improve the accuracy but we slow down the convergence, as is visible from the slopes in Figure 10. Here, the relative error is shown versus the number of iterations for different levels of discretization.

From these results, the proposed method appears to be reliable and efficient, and suitable for our purposes.

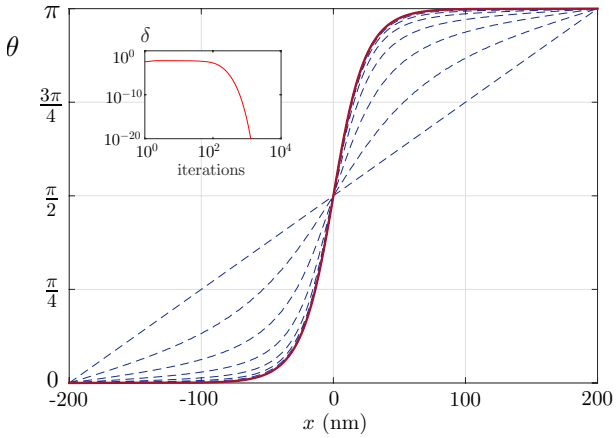

Fig. 8. Magnetization orientation distribution $\theta(x)$ converging toward the analytical solution (red curve) for the simple system with only exchange and anisotropy contributions. The iteration process starts from a linear guess. The inset shows the relative error versus the number of iterations.

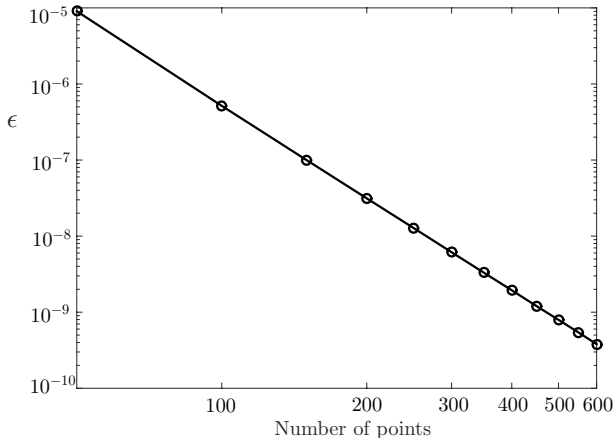

Fig. 9. Absolute error ϵ between numerical and theoretical solutions versus the number N of points used in the discretization (all simulations have been performed with the same stopping criterion based on $\delta_{\min} = 10^{-20}$).

4.2 Results

We now show some solutions of equation (30) by demonstrating the possibility to control the position of a domain wall within the nanostripe. To do this, as before, we use its discretized form shown in equation (32). With regard to the initial guess function utilized, we performed a first simulation with the relaxation method with $\sigma = 0$ starting from the linear guess between the boundary conditions. In this case the algorithm yields the magnetization profile in the ferromagnet when no stress is applied. This solution is then used as the initial guess function in simulations with

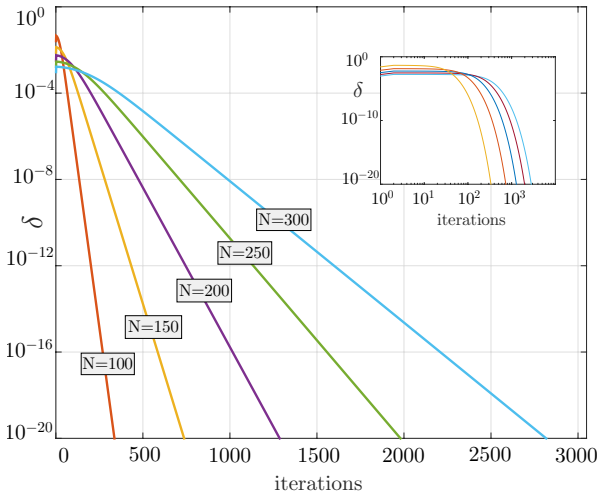

Fig. 10. Relative error δ as a function of the number of iterations for different values of N. In all cases, the convergence is definitively exponential. Moreover, for a larger number of points the convergence is slower.

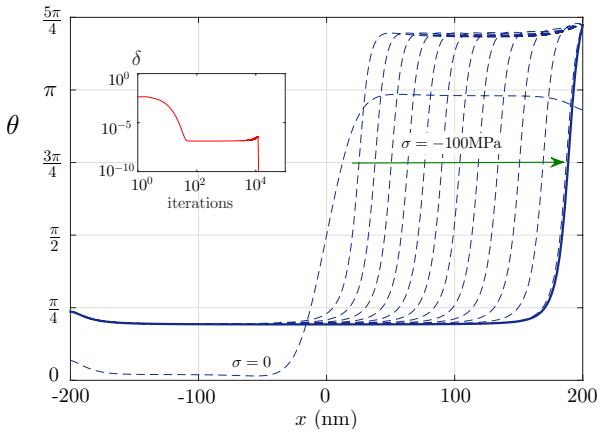

Fig. 11. Iterative process showing the ejection of the domain wall in a ferromagnet with constant rectangular section (h = 20 nm and ℓ = 40 nm). In the inset the relative error δ is plotted versus the iterations number. We used $\delta_{\min} = 10^{-10}$ and $\sigma = -100$ MPa.

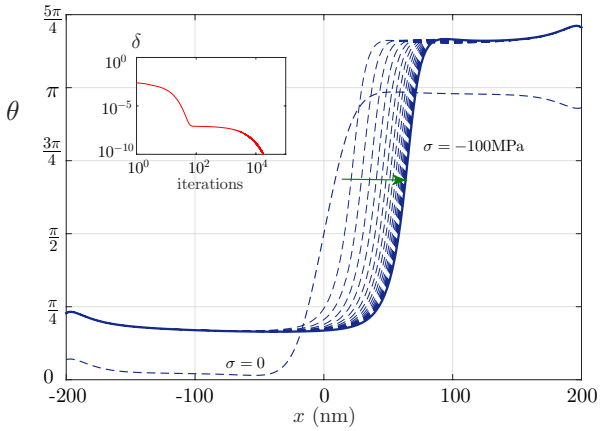

Fig. 12. Iterative process showing the path toward the equilibrium location of the domain wall for a parabolic nanostripe with central width a = 40 nm and width at extremities b = 70 nm (h = 20 nm). In the inset the relative error δ is plotted versus the iterations number. We used $\delta_{\min} = 10^{-10}$ and $\sigma = -100$ MPa.

applied stress $\sigma \neq 0$. This shows that the application of a stress to the nanostripe results in a change of equilibrium position for the domain wall in a direction dictated by the sign of σ. However, in the case of a nanostripe with constant cross-section, the domain wall reaches one stripe extremity, corresponding to domain wall ejection in a real experiment. For this reason, we propose to use a variable cross-section in order to have equilibrium positions within the length of the nanostripe with a smooth relation between applied stress and wall position.

Let us consider now a function $\ell(x)$ increasing with $|x|$ and minimal for $x = 0$, which is the initial location of the domain wall. Once the mechanical stress is applied, the domain wall will not reach the extremities, thanks to the exchange energy that grows with $|x|$. A new equilibrium position x_p is thus found and depends on the amplitude of the mechanical stress. It is interesting to notice that for larger σ, the domain wall will shift farther from the center, since the energy gap between the two domains widens. For high values of σ, the system exhibits a saturation of the domain wall position.

An example of wall ejection is shown in Figure 11 where we considered a uniform nanostripe with h = 20 nm, ℓ = 40 nm and L = 400 nm. We adopted the boundary conditions described by equation (31). The symmetrical curve between $-L/2$ and $+L/2$ represents the solution with $\sigma = 0$, used as initial guess for the iterative procedure when $\sigma = -100$ MPa. All the dashed lines represent iterations of the relaxation method. We plotted a curve every 1000 iterations to better show the evolution of the process and we used $\delta_{\min} = 10^{-10}$ for the stopping criterion. The domain wall arrives at the right extremity, eliminating the second magnetic domain (ejection). In the inset we also show the relative error δ versus the iteration number. We can identify two relaxation regime: in the first one the relative error decreases and the magnetization distribution assumes the correct shape (e.g., in terms of slope of the domain wall); in the second one the relative error is quite constant and the wall moves until ejection, corresponding to the final error drop.

In Figure 12 we observe an equilibrium position obtained in a nanostripe with variable (parabolic) cross-section. We considered a nanostripe with h = 20 nm and $\ell(x) = a + 4\frac{b-a}{L^2}x^2$ where $a = \ell(0)$ = 40 nm (central width), $b = \ell(\pm L/2)$ = 70 nm (width at extremities) and L = 400 nm. By starting with the same initial guess used in Figure 11, we apply $\sigma = -100$ MPa and we obtain a final position at about 60 nm. As before, we note two scaling regimes for the relative error, namely (i) attainment of the shape and (ii) displacement of the wall.

The magnetization distributions corresponding to different values of the applied stress are shown in Figure 13 together with the related energy distributions within the nanostripe. These results have been obtained with a profile $\ell(x)$ with a = 40 nm, b = 70 nm, h = 10 nm and

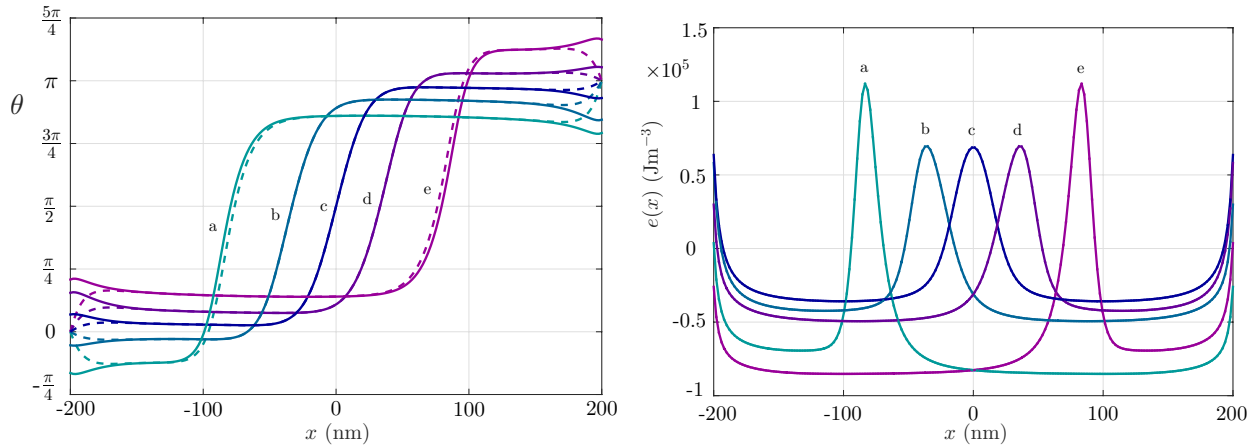

Fig. 13. Magnetization orientation distributions $\theta(x)$ (left) and corresponding energy profiles $e(x)$ (right) for several values of the applied stress σ: (a) $\sigma = 60$ MPa; (b) $\sigma = 20$ MPa; (c) $\sigma = 0$; (d) $\sigma = -20$ MPa; and (e) $\sigma = -60$ MPa. In the left panel solid lines correspond to solutions with boundary conditions calculated as in equation (31), whereas $\theta(-L/2) = 0$ and $\theta(+L/2) = \pi$ have been used for solutions represented with dashed lines.

$L = 400$ nm. In the left panel, concerning the magnetization distributions, the solid lines correspond to solutions obtained with the boundary conditions in equation (31) and the dashed lines to the boundary conditions $\theta(-L/2) = 0$ and $\theta(+L/2) = \pi$. Therefore, we can observe that the boundary conditions do not influence the overall behavior of the system. This is especially true for long wires and as long as there are two large and clearly defined domains. Indeed, the differences can be only observed in the regions close to the extremities. In the right panel we show the corresponding energy profiles $e(x)$ defined such that the total energy is $U = \int_{-L/2}^{+L/2} e(x)h\ell(x)dx$. It is not difficult to identify the regions corresponding to the two domains (with different energy densities) and the region related to the wall between them (peaks). It is interesting to note that the slope of the magnetization distribution of the wall (see left panel) is higher with stronger applied stress σ. It is coherent with the fact that the thickness of the wall (see right panel) is smaller with higher σ.

The knowledge of the magnetization distribution for several values of σ, as in Figure 13 (left panel), allows us to determine the position of the domain wall versus the applied stress, which represents the characteristic response of the system. We performed this analysis for three different structures as shown in Figure 14. In all cases we used a parabolic profile $\ell(x)$ defined by the parameter a and b, as before. The response exhibits a quite linear behavior for small values of σ and a saturation of the displacement for high values of σ. We underline that a larger section at the extremities of the nanostripe reduces the slope of the $x_p - \sigma$ curve and maximum displacement of the domain wall (it can be deduced by comparing the results for ℓ_2 and ℓ_3). This is due to the total exchange energy associated with the domain wall. Similarly, a larger thickness of the nanostripe reduces the slope of the curve and maximum displacement of the domain wall (it can be deduced by comparing the results for ℓ_1 and ℓ_2). This is due to the demagnetization energy, which is lower with thinner nanostripes.

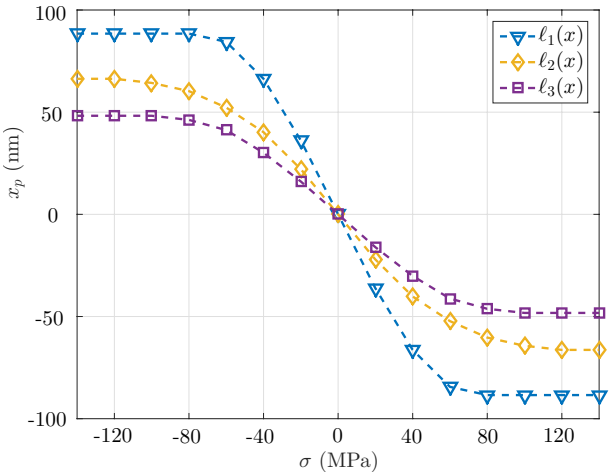

Fig. 14. Domain wall displacement as a function of the applied stress for three different quadratic profiles ℓ_1, ℓ_2 and ℓ_3 ($a_1 = a_2 = a_3 = 40$ nm, $b_1 = b_2 = 70$ nm, $b_3 = 80$ nm, $h_1 = 10$ nm, $h_2 = h_3 = 20$ nm). After a nearly linear region for low values of σ, the response saturates, exhibiting a displacement range depending on the geometry.

5 Conclusion

In this paper we presented a complete model describing the magnetization behavior in nanostripes with variable cross-section, subject to an external magnetic field and a mechanical stress. In particular, we wrote the equation governing the magnetization distribution by taking into account anisotropy, exchange, demagnetization, magnetostriction and Zeeman effects. The method applied consists in writing the total energy of the system in terms of the direction of the magnetization and then in applying the techniques of the calculus of variation in order to minimize the total energy itself. We also proposed an efficient numerical technique in order to solve the main nonlinear integro-differential equation with a relaxation, or iterative, method. We studied the convergence properties

of this algorithm by applying it to a particular case, which can be handled analytically. By means of our theoretical device, we demonstrated the possibility to control a magnetic domain wall position in a ferromagnetic nanostripe with external mechanical actions. This point is important for the applications since the mechanical stress to be applied can be generated through piezoelectric substrate. It means that the control of a magnetic domain wall position can be realized in multiferroic heterostructures (composed of piezoelectric and magnetoelastic subsystems) [24]. This technique is relevant from the energetic point of view. We can indeed draw a comparison with other methods based on the application of an external electric current. If we consider a piezoelectric substrate in our system, we obtain an energy $\Delta E = 1.5\times10^{-15}$ J for moving the wall between the left and right extreme positions. The details of the calculation can be found in reference [24]. In general, the total energy for moving the wall domain between two positions is the sum of the electrostatic energy stored within the piezoelectric substrate (CV^2) and the magnetic energy dissipated within the magnetoelastic stripe. Nevertheless, the latter is typically negligible and the total energy is approximately equal to the electrostatic contribution [35,36]. In this case we numerically proved that the magnetic dissipation ($\backsim 10^{-17}$ J) is two order of magnitude smaller than the electrostatic contribution ($\backsim 10^{-15}$ J), substantiating the previous statement.

For comparison, the energy consumption for one logic operation in a current-driven gate based on domain wall motion is $\Delta E = 10^4$ fJ [58]. Further investigations on this subject will consist in analyzing the dynamic behavior of the system [59–61] and the effects of thermal noise on the dynamics [62], as well as studying these phenomena at the experimental level.

Author contribution statement

T.M. and S.G. conceived the project. T.M. developed the numerical approach, performed the simulations and the data analysis. S.G. elaborated the theoretical framework and calculations. Y.D. and N.T. contributed in discussing the physical mechanisms and studied the technological feasibility and potential. T.M., S.G., Y.D. and N.T. prepared the manuscript. V.P. and P.P. supervised the project and discussed the methodologies. All authors discussed the results.

Appendix A: Variational approach to micromagnetism

The minimization of the functional U defined in equation (6) can be performed as follows

$$\min_{\boldsymbol{\gamma}\,:\,\|\boldsymbol{\gamma}\|=1} U \rightarrow \min_{\boldsymbol{\gamma}} \left[U + \int_V \lambda\,(\boldsymbol{\gamma}\cdot\boldsymbol{\gamma} - 1)\, dv \right], \qquad \text{(A.1)}$$

where $\lambda = \lambda(\boldsymbol{r})$ is a Lagrange multiplier introduced to fix the norm of the unit vector $\boldsymbol{\gamma}$. Therefore, we have to minimize

$$U' = \int_V \left[u_{an} + u_{ex} + u_{me} + \lambda\boldsymbol{\gamma}\cdot\boldsymbol{\gamma} \underbrace{-\mu_0 M_S\, \boldsymbol{H_L}\cdot\boldsymbol{\gamma}}_{u_{Ze}} \right] dv, \qquad \text{(A.2)}$$

with $\boldsymbol{H}_L$ fixed. This functional assumes its extremal value when

$$\frac{d}{d\alpha}\, U'\left[\boldsymbol{\gamma}(\boldsymbol{r}) + \alpha\boldsymbol{h}(\boldsymbol{r})\right]\Big|_{\alpha=0} = 0 \qquad \forall\, \boldsymbol{h}(\boldsymbol{r}), \qquad \text{(A.3)}$$

where the left-hand side represents the Gâteaux derivative of the functional U' [54]. If we define the quantity $U''(\boldsymbol{\gamma}) = U'(\boldsymbol{\gamma}) - \int_V u_{Ze} dv$, equation (A.3) can be rewritten as

$$\frac{d}{d\alpha}\, U''\left[\boldsymbol{\gamma} + \alpha\boldsymbol{h}\right]\Big|_{\alpha=0} - \frac{d}{d\alpha}\int_V \mu_0 M_S\, \boldsymbol{H}_L\cdot(\boldsymbol{\gamma} + \alpha\boldsymbol{h})\, dv\Big|_{\alpha=0} = 0, \qquad \text{(A.4)}$$

or, equivalently, as

$$\frac{d}{d\alpha}\, U''\left[\boldsymbol{\gamma} + \alpha\boldsymbol{h}\right]\Big|_{\alpha=0} - \int_V \mu_0 M_S\, \boldsymbol{H}_L\cdot\boldsymbol{h}\, dv = 0. \qquad \text{(A.5)}$$

Although in implicit form, this is the equation giving $\boldsymbol{\gamma}(\boldsymbol{r})$ in V. At this point, we can combine it with $\boldsymbol{H}_L = \boldsymbol{H}_0 + \boldsymbol{H}_d$. It is important to note that this subsitution cannot be made in U or U', before the minimization, since $\boldsymbol{H_d}$ is a function of $\boldsymbol{\gamma}$. Anyway, equation (A.5) becomes

$$\frac{d}{d\alpha}\, U''\left[\boldsymbol{\gamma} + \alpha\boldsymbol{h}\right]\Big|_{\alpha=0} - \int_V \mu_0 M_S\, \boldsymbol{H}_0\cdot\boldsymbol{h}\, dv - \int_V\int_V \mu_0 M_S^2\, \boldsymbol{h}(\boldsymbol{r})\cdot\hat{N}(\boldsymbol{r},\boldsymbol{r}_0)\boldsymbol{\gamma}(\boldsymbol{r}_0)\, d\boldsymbol{r}_0 d\boldsymbol{r} = 0, \qquad \text{(A.6)}$$

where we used equation (7) for the demagnetization field. Equivalently, we can also write

$$\frac{d}{d\alpha}U''\left[\boldsymbol{\gamma}+\alpha\boldsymbol{h}\right]\Big|_{\alpha=0} - \frac{d}{d\alpha}\int_V \mu_0 M_S\, \boldsymbol{H}_0\cdot(\boldsymbol{\gamma}+\alpha\boldsymbol{h})\, dv\Big|_{\alpha=0} - \frac{d}{d\alpha}\,\frac{1}{2}\int_V\int_V \mu_0 M_S^2\, \left[\boldsymbol{\gamma}(\boldsymbol{r}) + \alpha\boldsymbol{h}(\boldsymbol{r})\right] \cdot\hat{N}(\boldsymbol{r},\boldsymbol{r}_0)\left[\boldsymbol{\gamma}(\boldsymbol{r}_0) + \alpha\boldsymbol{h}(\boldsymbol{r}_0)\right]\, d\boldsymbol{r}_0 d\boldsymbol{r}\Big|_{\alpha=0} = 0, \qquad \text{(A.7)}$$

where we used the symmetries described in equations (9a) and (9b). We can then define an auxiliary function $\tilde{U}'$

$$\tilde{U}' = U''(\boldsymbol{\gamma}) - \int_V \mu_0 M_S\, \boldsymbol{H}_0\cdot\boldsymbol{\gamma}\, dv - \int_V\int_V \frac{1}{2}\mu_0 M_S^2 \boldsymbol{\gamma}(\boldsymbol{r})\cdot\hat{N}(\boldsymbol{r},\boldsymbol{r}_0)\boldsymbol{\gamma}(\boldsymbol{r}_0)\, d\boldsymbol{r}_0 d\boldsymbol{r}, \qquad \text{(A.8)}$$

which can be minimized with $\boldsymbol{H}_0$ fixed. We have therefore proved this series of equivalences

$$\min_{\boldsymbol{\gamma}:\|\boldsymbol{\gamma}\|=1} U\Big|_{\boldsymbol{H_L}\text{ fixed}} \Leftrightarrow \min_{\boldsymbol{\gamma}} U'\Big|_{\boldsymbol{H_L}\text{ fixed}} \Leftrightarrow \min_{\boldsymbol{\gamma}} \tilde{U}'\Big|_{\boldsymbol{H_0}\text{ fixed}} \Leftrightarrow \min_{\boldsymbol{\gamma}:\|\boldsymbol{\gamma}\|=1} \tilde{U}\Big|_{\boldsymbol{H_0}\text{ fixed}}, \quad \text{(A.9)}$$

where $\tilde{U}$ is defined in equation (11). Finally, the minimization of $\tilde{U}$ with respect to the direction $\boldsymbol{\gamma}$, with $\hat{T}$ and $\boldsymbol{H_0}$ imposed, leads to the actual magnetization of the ferromagnetic body. We can therefore apply the methods of the calculus of variations to obtain the equation for $\boldsymbol{\gamma}$. As before, we work with the Gâteaux derivative

$$\frac{d}{d\alpha}\,\tilde{U}'\left(\boldsymbol{\gamma}+\alpha\boldsymbol{h}\right)\Big|_{\alpha=0} = 0, \quad \text{(A.10)}$$

where

$$\tilde{U}'(\boldsymbol{\gamma}) = \tilde{U} + \int_V \lambda(\boldsymbol{r})(\boldsymbol{\gamma}\cdot\boldsymbol{\gamma}-1)\,dv. \quad \text{(A.11)}$$

We obtain

$$\begin{aligned} 0 = \int_V \Bigg[&\frac{\partial\phi}{\partial\boldsymbol{\gamma}}\cdot\boldsymbol{h} - \frac{1}{2}\alpha_{ij}\left(\frac{\partial h_l}{\partial x_i}\frac{\partial\gamma_l}{\partial x_j}+\frac{\partial\gamma_l}{\partial x_i}\frac{\partial h_l}{\partial x_j}\right) + 2\lambda h_l\gamma_l \\ &- \mu_0 M_S H_{0i} h_i - a_{iklm}T_{ik}(h_l\gamma_m+\gamma_l h_m)\Bigg]\,dv \\ &-\mu_0 M_s^2 \int_V\int_V N_{ij}(\boldsymbol{r},\boldsymbol{r_0})h_i(\boldsymbol{r})\gamma_j(\boldsymbol{r_0})d\boldsymbol{r_0}d\boldsymbol{r}, \end{aligned} \quad \text{(A.12)}$$

where we used again both symmetries of tensor $\hat{N}$. To proceed from here, we use the divergence theorem in the form

$$\int_V \frac{\partial\Phi}{\partial x_i}\,dv = \int_{\partial V} \Phi\, n_i\, dS. \quad \text{(A.13)}$$

Now, if $\Phi = fg$, we have

$$\int_V f\frac{\partial g}{\partial x_i}dv = \int_{\partial V} fg\, n_i\, dS - \int_V g\frac{\partial f}{\partial x_i}dv. \quad \text{(A.14)}$$

This property can be used to further elaborate equation (A.12), as follows

$$\begin{aligned} 0 = \int_V \Bigg[&\frac{\partial\phi}{\partial\boldsymbol{\gamma}}\cdot\boldsymbol{h} - \alpha_{ij}h_l\frac{\partial^2\gamma_l}{\partial x_i\partial x_j} + 2\lambda h_l\gamma_l - \mu_0 M_S H_{0l}h_l \\ &- 2a_{iklm}T_{ik}h_l\gamma_m\Bigg]\,dv + \int_{\partial V}\alpha_{ij}h_l\frac{\partial\gamma_l}{\partial x_j}n_i\,dS \\ &-\mu_0 M_s^2\int_V\int_V N_{ij}(\boldsymbol{r},\boldsymbol{r_0})h_i(\boldsymbol{r})\gamma_j(\boldsymbol{r_0})d\boldsymbol{r_0}d\boldsymbol{r}, \end{aligned} \quad \text{(A.15)}$$

where we exploited the symmetry of tensor α_{ij}. Being equation (A.15) true for any smooth function $h \in \mathbb{R}^3$, we can write

$$\begin{aligned} 0 = &\frac{\partial\phi}{\partial\boldsymbol{\gamma}} - \alpha_{ij}\frac{\partial^2\boldsymbol{\gamma}}{\partial x_i\partial x_j} - \mu_0 M_S\boldsymbol{H}_0 \\ &+2\lambda\boldsymbol{\gamma} - \mu_0 M_S\boldsymbol{H}_d - 2\hat{a}:\hat{T}\boldsymbol{\gamma}, \end{aligned} \quad \text{(A.16)}$$

where $\left(\hat{a}:\hat{T}\boldsymbol{\gamma}\right)_l = a_{iklm}T_{ik}\gamma_m$. The Lagrange multiplier λ can be finally eliminated by applying a cross-product with $\boldsymbol{\gamma}$, which yields equations (12) and (13).

From equation (A.15), we can also deduce the boundary conditions which can be applied to minimize the energy functional: $\alpha_{ij}h_l\frac{\partial\gamma_l}{\partial x_j}n_i = 0$ on ∂V, where the perturbation vector $\boldsymbol{h}$ is not free since it must verify the condition $(\boldsymbol{\gamma}+\alpha\boldsymbol{h})\cdot(\boldsymbol{\gamma}+\alpha\boldsymbol{h}) = 1$ when $\boldsymbol{\gamma}\cdot\boldsymbol{\gamma} = 1$. To the first order in α this translates to $\boldsymbol{\gamma}\cdot\boldsymbol{h} = 0$ and, therefore, we can say that $\boldsymbol{h} = \boldsymbol{w}\times\boldsymbol{\gamma}$ for an arbitrary vector $\boldsymbol{w}$. Then, $\boldsymbol{h}$ is not arbitrary but $\boldsymbol{w}$ is completely free. By considering $h_l = \epsilon_{lst}w_s\gamma_t$, we have $\alpha_{ij}\epsilon_{lst}w_s\gamma_t\frac{\partial\gamma_l}{\partial x_j}n_i = 0\ \forall w_s$, or $\alpha_{ij}\epsilon_{lst}\gamma_t\frac{\partial\gamma_l}{\partial x_j}n_i = 0\ \forall s$ on ∂V (ϵ_{lst} being the Levi-Civita permutation symbol). This condition can be strongly simplified when $\alpha_{ij}\propto\delta_{ij}$ (isotropic exchange). In this case we have $\epsilon_{lst}\gamma_t\frac{\partial\gamma_l}{\partial x_i}n_i = 0\ \forall s$, where $\frac{\partial\gamma_l}{\partial x_i}n_i$ is the directional derivative of γ_l along $\boldsymbol{n}$. So, it corresponds to $\boldsymbol{\gamma}\times\frac{\partial\boldsymbol{\gamma}}{\partial n} = 0$. We also observe that $\boldsymbol{\gamma}$ is always perpendicular to $\frac{\partial\boldsymbol{\gamma}}{\partial n}$ since $\|\boldsymbol{\gamma}\| = 1$. Therefore, in order to impose $\boldsymbol{\gamma}\times\frac{\partial\boldsymbol{\gamma}}{\partial n} = 0$, it is sufficient to have $\frac{\partial\boldsymbol{\gamma}}{\partial n} = 0$ on ∂V.

Appendix B: Calculation of the demagnetization field

We provide here a technique to numerically evaluate the demagnetization field in our system. To begin, we consider equation (7) giving the demagnetization field for an arbitrary region V. In analogy with the theory of the electric dipole [42], we may introduce a magnetic scalar potential Φ such that

$$\boldsymbol{H}_d(\boldsymbol{r}) = -\boldsymbol{\nabla}\Phi, \quad \text{(B.1)}$$

where

$$\Phi(\boldsymbol{r}) = \int_V \frac{1}{4\pi}\frac{\boldsymbol{M}(\boldsymbol{r_0})\cdot(\boldsymbol{r}-\boldsymbol{r_0})}{\|\boldsymbol{r}-\boldsymbol{r_0}\|^3}d\boldsymbol{r_0}. \quad \text{(B.2)}$$

A useful development can be performed when the magnetization $\boldsymbol{M}$ is uniform in a given region. In this case we can apply the divergence theorem

$$\int_V \operatorname{div}\boldsymbol{w}\,dv = \int_{\partial V}\boldsymbol{w}\cdot\boldsymbol{n}\,dS, \quad \text{(B.3)}$$

where we consider $\boldsymbol{w} = \frac{\boldsymbol{M}}{\|\boldsymbol{r}-\boldsymbol{r_0}\|}$, with a constant field $\boldsymbol{M}$. Indeed, we obtain

$$\operatorname{div}\boldsymbol{w} = \boldsymbol{M}\cdot\boldsymbol{\nabla}\frac{1}{\|\boldsymbol{r}-\boldsymbol{r_0}\|} = \boldsymbol{M}\cdot\frac{\boldsymbol{r}-\boldsymbol{r_0}}{\|\boldsymbol{r}-\boldsymbol{r_0}\|^3}, \quad \text{(B.4)}$$

and, therefore, equation (B.3) reads

$$\int_V \boldsymbol{M}\cdot\frac{\boldsymbol{r}-\boldsymbol{r}_0}{\|\boldsymbol{r}-\boldsymbol{r}_0\|^3}\,dv=\int_{\partial V}\frac{\boldsymbol{M}\cdot\boldsymbol{n}}{\|\boldsymbol{r}-\boldsymbol{r}_0\|}\,dS. \tag{B.5}$$

As a conclusion, for a uniform magnetization $\boldsymbol{M}$, the scalar potential is given by

$$\Phi(\boldsymbol{r})=\frac{1}{4\pi}\boldsymbol{M}\cdot\int_{\partial V}\frac{\boldsymbol{n}\,dS}{\|\boldsymbol{r}-\boldsymbol{r}_0\|}, \tag{B.6}$$

where $\boldsymbol{n}$ is the unit vector normal to the external surface ∂V with area element dS. To calculate the total demagnetization field in a given point, we can partition the whole region in a given number of parallelepipedal layers. As discussed below, the parallelepipedal geometry allows for quick and simple computation of the demagnetization field through the scalar potential Φ. Then, we can add all the contributions to get the final result. Hence, we suppose $\boldsymbol{M}$ uniform within the arbitrary parallelepiped $[x_1,x_2]\times[y_1,y_2]\times[z_1,z_2]$, and we calculate Φ through equation (B.6). We define the integral $\boldsymbol{I}=\int_{\partial V}\frac{\boldsymbol{n}\,dS}{\|\boldsymbol{r}-\boldsymbol{r}_0\|}$ and we write the x component as

$$\begin{aligned}I_x=&\int_{z_1}^{z_2}\int_{y_1}^{y_2}\frac{dy_0\,dz_0}{\sqrt{(x-x_2)^2+(y-y_0)^2+(z-z_0)^2}}\\&-\int_{z_1}^{z_2}\int_{y_1}^{y_2}\frac{dy_0\,dz_0}{\sqrt{(x-x_1)^2+(y-y_0)^2+(z-z_0)^2}}.\end{aligned} \tag{B.7}$$

A change of variables leads to

$$\begin{aligned}I_x=&\int_{z-z_1}^{z-z_2}\int_{y-y_1}^{y-y_2}\frac{d\xi d\eta}{\sqrt{(x-x_2)^2+\xi^2+\eta^2}}\\&-\int_{z-z_1}^{z-z_2}\int_{y-y_1}^{y-y_2}\frac{d\xi d\eta}{\sqrt{(x-x_1)^2+\xi^2+\eta^2}}.\end{aligned} \tag{B.8}$$

Now, let us define the function $\mathcal{F}(A,B,C,D,E,F)$ as

$$\mathcal{F}=\int_A^B\int_C^D\left[\frac{1}{\sqrt{E^2+\xi^2+\eta^2}}-\frac{1}{\sqrt{F^2+\xi^2+\eta^2}}\right]d\xi d\eta, \tag{B.9}$$

and we obtain the demagnetization potential in the form

$$\Phi(\boldsymbol{r})=\frac{1}{4\pi}\left[M_xI_x+M_yI_y+M_zI_z\right], \tag{B.10}$$

where

$$I_x=\mathcal{F}(z-z_1,z-z_2,y-y_1,y-y_2,x-x_1,x-x_2), \tag{B.11}$$

$$I_y=\mathcal{F}(x-x_1,x-x_2,z-z_1,z-z_2,y-y_1,y-y_2), \tag{B.12}$$

$$I_z=\mathcal{F}(y-y_1,y-y_2,x-x_1,x-x_2,z-z_1,z-z_2). \tag{B.13}$$

To lighten the notation, we chose to write it in more concise form

$$\Phi(\boldsymbol{r})=\frac{1}{4\pi}\left[M_x\mathcal{F}\Big|_{321}+M_y\mathcal{F}\Big|_{132}+M_z\mathcal{F}\Big|_{213}\right], \tag{B.14}$$

where the symbol $\mathcal{F}\Big|_{ijk}$ means that the function $\mathcal{F}$ is calculated with variables specified in equations (B.11)–(B.13). Finally, the components of the demagnetization field can be derived as

$$\begin{aligned}H_{dx}=-\frac{\partial\Phi}{\partial x}=-\frac{1}{4\pi}\Bigg[&M_x\left(\frac{\partial\mathcal{F}}{\partial E}\Big|_{321}+\frac{\partial\mathcal{F}}{\partial F}\Big|_{321}\right)\\&+M_y\left(\frac{\partial\mathcal{F}}{\partial A}\Big|_{132}+\frac{\partial\mathcal{F}}{\partial B}\Big|_{132}\right)\\&+M_z\left(\frac{\partial\mathcal{F}}{\partial C}\Big|_{213}+\frac{\partial\mathcal{F}}{\partial D}\Big|_{213}\right)\Bigg],\end{aligned} \tag{B.15}$$

$$\begin{aligned}H_{dy}=-\frac{\partial\Phi}{\partial y}=-\frac{1}{4\pi}\Bigg[&M_x\left(\frac{\partial\mathcal{F}}{\partial C}\Big|_{321}+\frac{\partial\mathcal{F}}{\partial D}\Big|_{321}\right)\\&+M_y\left(\frac{\partial\mathcal{F}}{\partial E}\Big|_{132}+\frac{\partial\mathcal{F}}{\partial F}\Big|_{132}\right)\\&+M_z\left(\frac{\partial\mathcal{F}}{\partial A}\Big|_{213}+\frac{\partial\mathcal{F}}{\partial B}\Big|_{213}\right)\Bigg],\end{aligned} \tag{B.16}$$

$$\begin{aligned}H_{dz}=-\frac{\partial\Phi}{\partial z}=-\frac{1}{4\pi}\Bigg[&M_x\left(\frac{\partial\mathcal{F}}{\partial A}\Big|_{321}+\frac{\partial\mathcal{F}}{\partial B}\Big|_{321}\right)\\&+M_y\left(\frac{\partial\mathcal{F}}{\partial C}\Big|_{132}+\frac{\partial\mathcal{F}}{\partial D}\Big|_{132}\right)\\&+M_z\left(\frac{\partial\mathcal{F}}{\partial E}\Big|_{213}+\frac{\partial\mathcal{F}}{\partial F}\Big|_{213}\right)\Bigg].\end{aligned} \tag{B.17}$$

In equation (30), we are working with a two-dimensional problem where $M_z=0$ and, therefore, the number of necessary components to compute $\boldsymbol{H}_d$ is reduced. Moreover, the symmetry in equation (9a) allows us to prove that the operator relating $\boldsymbol{H}_d$ and $\boldsymbol{M}$ is always symmetric. Indeed, we have

$$\frac{\partial\mathcal{F}}{\partial A}\Big|_{132}+\frac{\partial\mathcal{F}}{\partial B}\Big|_{132}=\frac{\partial\mathcal{F}}{\partial C}\Big|_{321}+\frac{\partial\mathcal{F}}{\partial D}\Big|_{321}, \tag{B.18}$$

a property which further reduces the complexity of equations (B.15) and (B.16)

$$\begin{aligned}H_{dx}=-\frac{1}{4\pi}\Bigg[&M_x\left(\frac{\partial\mathcal{F}}{\partial E}\Big|_{321}+\frac{\partial\mathcal{F}}{\partial F}\Big|_{321}\right)\\&+M_y\left(\frac{\partial\mathcal{F}}{\partial A}\Big|_{132}+\frac{\partial\mathcal{F}}{\partial B}\Big|_{132}\right)\Bigg],\end{aligned} \tag{B.19}$$

$$\begin{aligned}H_{dy}=-\frac{1}{4\pi}\Bigg[&M_x\left(\frac{\partial\mathcal{F}}{\partial A}\Big|_{132}+\frac{\partial\mathcal{F}}{\partial B}\Big|_{132}\right)\\&+M_y\left(\frac{\partial\mathcal{F}}{\partial E}\Big|_{132}+\frac{\partial\mathcal{F}}{\partial F}\Big|_{132}\right)\Bigg].\end{aligned} \tag{B.20}$$

To complete this discussion, one can observe that the integral in equation (B.9) can be calculated in closed form. This is very useful for the numerical implementation of the proposed procedure

$$\begin{aligned}\mathcal{F} = &+A\,\ln\frac{\sqrt{E^2+A^2+D^2}+D}{\sqrt{F^2+A^2+D^2}+D}\frac{\sqrt{F^2+A^2+C^2}+C}{\sqrt{E^2+A^2+C^2}+C}\\ &+B\,\ln\frac{\sqrt{E^2+B^2+C^2}+C}{\sqrt{F^2+B^2+C^2}+C}\frac{\sqrt{F^2+B^2+D^2}+D}{\sqrt{E^2+B^2+D^2}+D}\\ &+C\,\ln\frac{\sqrt{E^2+A^2+C^2}-A}{\sqrt{F^2+A^2+C^2}-A}\frac{\sqrt{F^2+B^2+C^2}-B}{\sqrt{E^2+B^2+C^2}-B}\\ &+D\,\ln\frac{\sqrt{E^2+B^2+D^2}-B}{\sqrt{F^2+B^2+D^2}-B}\frac{\sqrt{F^2+A^2+D^2}-A}{\sqrt{E^2+A^2+D^2}-A}\\ &+E\,\arctan\left(\frac{E^2+A^2-A\sqrt{E^2+A^2+D^2}}{D\,E}\right)\\ &-E\,\arctan\left(\frac{E^2+A^2-A\sqrt{E^2+A^2+C^2}}{C\,E}\right)\\ &-E\,\arctan\left(\frac{E^2+B^2-B\sqrt{E^2+B^2+D^2}}{D\,E}\right)\\ &+E\,\arctan\left(\frac{E^2+B^2-B\sqrt{E^2+B^2+C^2}}{C\,E}\right)\\ &-F\,\arctan\left(\frac{F^2+A^2-A\sqrt{F^2+A^2+D^2}}{D\,F}\right)\\ &+F\,\arctan\left(\frac{F^2+A^2-A\sqrt{F^2+A^2+C^2}}{C\,F}\right)\\ &+F\,\arctan\left(\frac{F^2+B^2-B\sqrt{F^2+B^2+D^2}}{D\,F}\right)\\ &-F\,\arctan\left(\frac{F^2+B^2-B\sqrt{F^2+B^2+C^2}}{C\,F}\right).\end{aligned} \tag{B.21}$$

Moreover, all its derivatives can be computed in order to implement equations (B.15)–(B.17). This can be easily done, e.g., in a symbolic environment. A similar calculation can be also found in reference [63].

Appendix C: Domain wall with exchange and anisotropy energy

We analyze a specific domain wall configuration, which is important from both the theoretical and numerical points of view. We consider the simple case of a ferromagnetic stripe with only exchange and anisotropy energy contributions. Accordingly, the total energy can be deduced from equation (26), eventually obtaining

$$U = hl\int_{-\frac{L}{2}}^{+\frac{L}{2}}\left[-K_u\cos^2\theta + A\left(\frac{d\theta}{dx}\right)^2\right]dx. \tag{C.1}$$

The Lagrangian function of the variational problem is therefore

$$\mathcal{L} = -K_u\cos^2\theta + A\theta'^2, \tag{C.2}$$

where $\theta' \equiv \frac{d\theta}{dx}$. The associated Hamiltonian function is

$$\mathcal{H} = \frac{\partial\mathcal{L}}{\partial\theta'}\theta' - \mathcal{L} = A\theta'^2 + K_u\cos^2\theta. \tag{C.3}$$

Since $\frac{\partial\mathcal{L}}{\partial x} = 0$, we have the conservation of $\mathcal{H}$, leading to the simplified differential equation

$$\theta' = \sqrt{-\frac{K_u}{A}\cos^2\theta + C_1}, \tag{C.4}$$

where C_1 is an integration constant. The boundary conditions

$$\theta\left(-\frac{L}{2}\right) = 0, \quad \theta\left(+\frac{L}{2}\right) = \pi, \tag{C.5}$$

adopted to analyze the problem, guarantee the existence of the ferromagnetic domain wall. Separating the variables in equation (C.4), we obtain

$$\int_0^{\theta}\frac{d\theta}{\sqrt{C_2+\sin^2\theta}} = \left(x+\frac{L}{2}\right)\sqrt{\frac{K_u}{A}}, \tag{C.6}$$

where we used the first boundary condition and we introduced $C_2 = AC_1/K_u - 1$. The coefficient C_2 can be calculated by considering the second boundary condition. We get

$$\int_0^{\pi}\frac{d\theta}{\sqrt{C_2+\sin^2\theta}} = 2\int_0^{\frac{\pi}{2}}\frac{d\theta}{\sqrt{C_2+\sin^2\theta}} = L\sqrt{\frac{K_u}{A}}. \tag{C.7}$$

We now introduce the integral [64]

$$\int\frac{dx}{\sqrt{1+p^2\sin^2 x}} = \frac{1}{\sqrt{1+p^2}}F\left(\alpha, \frac{p}{\sqrt{1+p^2}}\right), \tag{C.8}$$

where $\alpha = \arcsin\frac{\sqrt{1+p^2}\sin x}{\sqrt{1+p^2\sin x}}$ and $F(\nu,q)$ is the incomplete elliptic integral of the first kind, defined as [65,66]

$$F(\nu,q) = \int_0^{\nu}\frac{du}{\sqrt{1-q^2\sin^2 u}} = \int_0^{\sin\nu}\frac{dx}{\sqrt{(1-x^2)(1-q^2x^2)}}. \tag{C.9}$$

We therefore obtain the equation for C_2 in the form

$$\frac{1}{\sqrt{1+C_2}}K\left(\frac{1}{\sqrt{1+C_2}}\right)=\frac{L}{2}\sqrt{\frac{K_u}{A}}, \tag{C.10}$$

where we also used the complete elliptic integral of the first kind $K(q)$ [65,66]

$$K(q)=F\left(\frac{\pi}{2},q\right)=\int_0^{\frac{\pi}{2}}\frac{du}{\sqrt{1-q^2\sin^2 u}}. \tag{C.11}$$

Similarly, we can rewrite equation (C.6) in terms of elliptic integrals

$$\sqrt{\frac{K_u}{A}}\left(x+\frac{L}{2}\right)=\frac{1}{\sqrt{1+C_2}}F\left(\alpha_\theta,\frac{1}{\sqrt{1+C_2}}\right) \tag{C.12}$$

where

$$\alpha_\theta=\arcsin\frac{\sqrt{1+C_2}\sin\theta}{\sqrt{C_2+\sin^2\theta}}. \tag{C.13}$$

Equations (C.10) and (C.12), although in implicit form, solve the problem of the finite-length stripe with exchange and anisotropy energies. We finally observe that by defining $\xi=\sqrt{1+C_2}$, these equations can be further simplified as follows

$$\sqrt{\frac{K_u}{A}}\left(x+\frac{L}{2}\right)=\frac{1}{\xi}F\left(\arcsin\frac{\xi\sin\theta}{\sqrt{\xi^2-\cos^2\theta}},\frac{1}{\xi}\right), \tag{C.14}$$

$$\frac{1}{\xi}K\left(\frac{1}{\xi}\right)=\frac{L}{2}\sqrt{\frac{K_u}{A}}. \tag{C.15}$$

It is interesting to prove that, for $L\to\infty$, we obtain a classical result cited in several textbooks (see, e.g., Ref. [39]). To begin, we note that $\xi\to 1^+$ and therefore $\eta\equiv 1/\xi\to 1^-$ when $L\to\infty$. Equation (C.14), in terms of η, becomes

$$\sqrt{\frac{K_u}{A}}x+\eta K(\eta)=\eta F\left(\arcsin\frac{\sin\theta}{\sqrt{1-\eta^2\cos^2\theta}},\eta\right). \tag{C.16}$$

Hence, the limiting case for $L\to\infty$ is not trivial since both arguments of the elliptic function F in equation (C.16) depends on $\eta\to 1^-$. To cope with with this problem, we use the following property of the function F [65,66]

$$\begin{aligned}&F(\varphi,\sin\alpha)+F(\psi,\sin\alpha)=K(\sin\alpha)\\&\text{if}\quad\cos\alpha\tan\varphi\tan\psi=1,\end{aligned} \tag{C.17}$$

with $\sin\alpha=\eta$ and $\varphi=\arcsin\frac{\sin\theta}{\sqrt{1-\eta^2\cos^2\theta}}$. Then equation (C.16) can be eventually rewritten as

$$\sqrt{\frac{K_u}{A}}x+\eta F(\psi,\eta)=0, \tag{C.18}$$

where ψ can be found through the relation

$$\tan\psi=\frac{1}{\cos\alpha\tan\varphi}=\frac{\sqrt{1-\eta^2\cos^2\theta-\sin^2\theta}}{\sin\theta\sqrt{1-\eta^2}}, \tag{C.19}$$

leading to $\sin\psi=\cos\theta$. Consequently, equation (C.18) reduces to $\sqrt{\frac{K_u}{A}}x+\eta F(\arcsin\cos\theta,\eta)=0$. Therefore, for $L\to\infty$ (i.e. $\eta\to 1$), we have that $\sqrt{\frac{K_u}{A}}x+\eta F(\arcsin\cos\theta,1)=0$. Now, we use the property [65,66]

$$F(\psi,1)=\ln(\sec\psi+\tan\psi), \tag{C.20}$$

and we can easily obtain the result

$$\begin{aligned}\theta(x)&=2\arctan\left[\exp\left(\sqrt{\frac{K_u}{A}}x\right)\right]\\&=\pi-\arccos\left[\tanh\left(\sqrt{\frac{K_u}{A}}x\right)\right],\end{aligned} \tag{C.21}$$

which is the well-known solution for the infinitely long stripe with exchange and anisotropy energies [39].

References

1. D.A. Allwood, G. Xiong, C. Faulkner, D. Atkinson, D. Petit, R.P. Cowburn, Science, **309**, 1688 (2005)
2. S.S. Parkin, M. Hayashi, L. Thomas, Science **320**, 190 (2008)
3. T. Ono, H. Miyajima, K. Shigeto, K. Mibu, N. Hosoito, T. Shinjo, Science **284**, 468 (1999)
4. D. Atkinson, D.A. Allwood, G. Xiong, M.D. Cooke, C.C. Faulkner, R.P. Cowburn, Nat. Mater. **2**, 85 (2003)
5. G.S.D. Beach, C. Nistor, C. Knutson, M. Tsoi, J.L. Erskine, Nat. Mater. **4**, 741 (2005)
6. M. Hayashi, L. Thomas, C. Rettner, R. Moriya, Y.B. Bazaliy, S.S.P. Parkin, Phys. Rev. Lett. **98**, 037204 (2007)
7. D. Ravelosona, S. Mangin, J.A. Katine, E.E. Fullerton, B.D. Terris, Appl. Phys. Lett. **90**, 072508 (2007)
8. A.V. Khvalkovskiy, V. Cros, D. Apalkov, V. Nikitin, M. Krounbi, K.A. Zvezdin, A. Anane, J. Grollier, A. Fert, Phys. Rev. B **87**, 020402 (2013)
9. P.N. Skirdkov, K.A. Zvezdin, A.D. Belanovsky, J. Grollier, V. Cros, C.A. Ross, A.K. Zvezdin, Appl. Phys. Lett. **104**, 242401 (2014)
10. J. Dean, M.T. Bryan, T. Schrefl, D.A. Allwood, J. Appl. Phys. **109**, 023915 (2011)
11. M.T. Bryan, J. Dean, D.A. Allwood, Phys. Rev. B **85**, 144411 (2012)
12. N. Lei, T. Devolder, G. Agnus, P. Aubert, L. Daniel, J.-V. Kim, W. Zhao, T. Trypiniotis, R.P. Cowburn, C. Chappert, D. Ravelosona, P. Lecoeur, Nat. Commun. **4**, 1378 (2013)
13. B. Van de Wiele, L. Laurson, K.J.A. Franke, S. van Dijken, Appl. Phys. Lett. **104**, 012401 (2014)
14. K.J.A. Franke, B. Van de Wiele, Y. Shirahata, S.J. Hämäläinen, T. Taniyama, S. van Dijken, Phys. Rev. X **5**, 011010 (2015)
15. R. Tolley, T. Liu, Y. Xu, S. Le Gall, M. Gottwald, T. Hauet, M. Hehn, F. Montaigne, E.E. Fullerton, S. Mangin, Appl. Phys. Lett. **106**, 242403 (2015)
16. E. De Ranieri, P.E. Roy, D. Fang, E.K. Vehsthedt, A.C. Irvine, D. Heiss, A. Casiraghi, R.P. Campion, B.L. Gallagher, T. Jungwirth, J.Wunderlich, Nat. Mater. **12**, 808 (2013)

17. G. Catalan, J. Seidel, R. Ramesh, J.F. Scott, Rev. Mod. Phys. **84**, 119 (2012)
18. M. Sharad, C. Augustine, G. Panagopoulos, K. Roy, IEEE Trans. Nanotechnol. **11**, 843 (2012)
19. B. Behin-Aein, D. Datta, S. Salahuddin, S. Datta, Nat. Nanotechnol. **5**, 266 (2010)
20. S. Parkin, S.-H. Yang, Nat. Nanotechnol. **10**, 195 (2015)
21. N. Locatelli, V. Cros, J. Grollier, Nat. Mater. **13**, 11 (2014)
22. H. Sohn, M.E. Nowakowski, C.Y. Liang, J.L. Hockel, K. Wetzlar, S. Keller, B.M. McLellan, M.A. Marcus, A. Doran, A. Young, M. Kläui, G.P. Carman, J. Bokor, R.N. Candler, ACS Nano **9**, 4814 (2015)
23. M. Kruzík, A. Prohl, SIAM Rev. **48**, 439 (2006)
24. T. Mathurin, S. Giordano, Y. Dusch, N. Tiercelin, P. Pernod, V. Preobrazhensky, Appl. Phys. Lett. **108**, 082401 (2016)
25. C.W. Nan, M.I. Bichurin, S. Dong, D. Viehland, G. Srinivasan, J. Appl. Phys. **103**, 031101 (2008)
26. S. Giordano, M. Goueygou, N. Tiercelin, A. Talbi, P. Pernod, V. Preobrazhensky, Int. J. Eng. Sci. **78**, 134 (2014)
27. S.-T. Gu, Q.-C. He, Philos. Mag. **95**, 2793, (2015)
28. S. Giordano, Mech. Res. Comm. **55**, 18 (2014)
29. N. Tiercelin, Y. Dusch, V. Preobrazhensky, P. Pernod, J. Appl. Phys. **109**, 07D726 (2011)
30. N. Tiercelin, Y. Dusch, A. Klimov, S. Giordano, V. Preobrazhensky, P. Pernod, Appl. Phys. Lett. **99**, 192507 (2011)
31. Y. Dusch, N. Tiercelin, A. Klimov, S. Giordano, V. Preobrazhensky, P. Pernod, J. Appl. Phys. **113**, 17C719 (2013)
32. Y. Dusch, V. Rudenko, N. Tiercelin, S. Giordano, V. Preobrazhensky, P. Pernod, Nanomater. Nanostruct. **2**, 44 (2012)
33. A.K. Biswas, S. Bandyopadhyay, J. Atulasimha, Appl. Phys. Lett. **104**, 232403 (2014)
34. S. Giordano, Y. Dusch, N. Tiercelin, P. Pernod, V. Preobrazhensky, Phys. Rev. B **85**, 155321 (2012)
35. S. Giordano, Y. Dusch, N. Tiercelin, P. Pernod, V. Preobrazhensky, J. Phys. D **46**, 325002 (2013)
36. N. Tiercelin, Y. Dusch, S. Giordano, A. Klimov, V. Preobrazhensky, P. Pernod, Strain Mediated Magnetoelectric Memory, in *Nanomagnetic and Spintronic Devices for Energy-Efficient Memory and Computing*, edited by S. Bandyopadhyay, J. Atulasimha (John Wiley & Sons Ltd., 2016)
37. K. Roy, S. Bandyopadhyay, J. Atulasimha, J. Appl. Phys. **112**, 023914 (2012)
38. H. Ahmad, J. Atulasimha, S. Bandyopadhyay, Sci. Rep. **5**, 18264 (2015)
39. L.D. Landau, E.M. Lifshitz, *Electrodynamics of Continuous Media* (Pergamon Press, London, 1984)
40. W.F. Brown, *Micromagnetics* (Interscience Publisher, New York, 1963)
41. W.F. Brown, *Magnetoelastic Interactions* (Springer-Verlag, Berlin, 1966)
42. J.A. Stratton, *Electromagnetic theory* (Mc Graw Hill, New York, 1941)
43. C. Miehe, G. Ethiraj, Comput. Methods Appl. Mech. Eng. **245**, 331 (2012)
44. G. Bertotti, I. Mayergoyz, C. Serpico, *Nonlinear Magnetization Dynamic in Nanosystems* (Elsevier, Oxford, 2000)
45. N.L. Schryer, L.R. Walker, J. Appl. Phys. **45**, 5406 (1974)
46. Y. Dusch, N. Tiercelin, A. Klimov, V. Rudenko, Y. Ignatov, S. Hage-Ali, P. Pernod, V. Preobrazhensky, J. Appl. Phys. **109**, 07A720 (2011)
47. P. Gaunt, Philos. Mag. **48**, 261 (1983)
48. T. Rojac, M. Kosec, B. Budic, N. Setter, D. Damjanovic, J. Appl. Phys. **108**, 074107 (2010)
49. D.I. Paul, J. Appl. Phys. **53**, 1649 (1982)
50. J.P. Attané, Y. Samson, A. Marty, D. Halley, C. Beigné, Appl. Phys. Lett. **79**, 794 (2001)
51. M. Kläui, C.A.F. Vaz, J. Rothman, J.A.C. Bland, W. Wernsdorfer, G. Faini, E. Cambril, Phys. Rev. Lett. **90**, 097202 (2003)
52. D. Petit, A.-V. Jausovec, D. Read, R.P. Cowburn, J. Appl. Phys. **103**, 114307 (2008)
53. M. Kläui, H. Ehrke, U. Rüdiger, T. Kasama, R.E. Dunin-Borkowski, D. Backes, L.J. Heyderman, C.A.F. Vaz, J.A.C. Bland, G. Faini, E. Cambril, W. Wernsdorfer, Appl. Phys. Lett. **87**, 102509 (2005)
54. A.N. Kolmogorov, S.V. Fomin, *Elements of the Theory of Functions and Functional Analysis* (Dover, New York, 1999)
55. D.B. Gopman, J.W. Lau, K.P. Mohanchandra, K. Wetzlar, G.P. Carman, Phys. Rev. B **93**, 064425 (2016)
56. Y.Y. Huang, Y.M. Jin, Appl. Phys. Lett. **93**, 142504 (2008)
57. H.B. Keller, *Numerical Solution of Two Point Boundary Value Problems* (SIAM, Philadelphia, 1976)
58. P. Xu, K. Xia, C. Gu, L. Tang, H. Yang, J. Li, Nat. Nanotechnol. **3**, 97 (2008)
59. L. Landau, E. Lifshitz, Phys. Zeitsch. der Sow. **8**, 153 (1935)
60. T.L. Gilbert, Phys. Rev. **100**, 1243 (1955) (abstract only)
61. T.L. Gilbert, IEEE Trans. Mag. **40**, 3443 (2004)
62. S. Giordano, Y. Dusch, N. Tiercelin, P. Pernod, V. Preobrazhensky, Eur. Phys. J. B **86**, 249 (2013)
63. R. Ravaud, G. Lemarquand, Prog. Electromagn. Res. B **98**, 207 (2009)
64. I.S. Gradshteyn, I.M. Ryzhik, *Table of Integrals, Series and Products* (Academic Press, San Diego, 1965)
65. M. Abramowitz, I.A. Stegun, *Handbook of Mathematical Functions* (Dover Publication, New York, 1970)
66. F.W.J. Olver, D.W. Lozier, R.F. Boisvert, C.W. Clark, *NIST Handbook of Mathematical Functions* (National Institute of Standards and Technology and Cambridge University Press, New York, 2010)